AFIT/GEO/ENG/93M-01

SELF-REFERENCED SPECKLE HOLOGRAPHY (SRSH)

IMAGE RECONSTRUCTION PERFORMANCE

THESIS

John Robert Levey

AFIT/GEO/ENG/93M-01

Approved for public release; Distribution unlimited

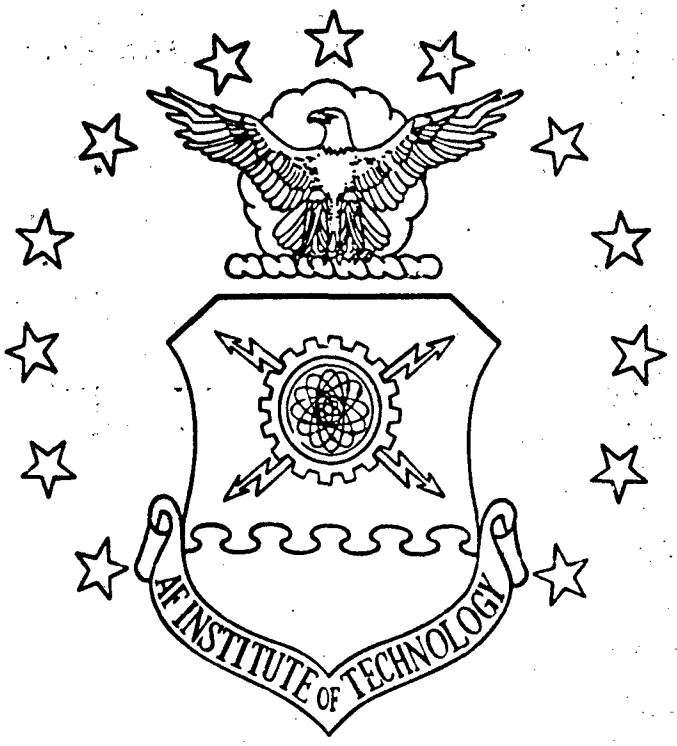

SELF REFERENCED SPECKLE HOLOGRAPHY (SRSH)

IMAGE RECONSTRUCTION PERFORMANCE

THESIS

[redacted]

AFIT/GEO/ENG/93M-01

DEPARTMENT OF THE AIR FORCE
AIR UNIVERSITY
AIR FORCE INSTITUTE OF TECHNOLOGY

Wright-Patterson Air Force Base, Ohio

AFIT/GEO/ENG/93M-01

SELF-REFERENCED SPECKLE HOLOGRAPHY (SRSH) IMAGE RECONSTRUCTION PERFORMANCE

THESIS

Presented to the Faculty of the School of Engineering

of the Air Force Institute of Technology

Air University

In Partial Fulfillment of the

Requirements for the Degree of

Master of Science in Electrical Engineering

John Robert Devey, B.S.E.E.,B.S.F.R

March, 1993

March 1993 Master's Thesis

Self-referenced speckle holography (SRSH) image reconstruction performance

John R. Devey

Air Force Institute of Technology, WPAFB OH 45433-6583 AFIT/GEO/ENG/93M-02

Captain Mike Roggemann
PL/LIMI
Kirtland AFB, NM 87117

Approved for public release; distribution unlimited

The Speckle Holography technique uses a series of short exposure images and associated wave front sensor measurements to reconstruct astronomical images. The reconstruction technique effectively boosts the amplitude of high spatial frequencies to allow for finer resolution of astronomical objects. A simulation package that calculates the optical transfer function (OTF) of a telescopic system was previously developed for the Phillips Laboratory. This software was modified slightly to provide the Speckle Holography system transfer function (STF) for a telescopic system under varying seeing conditions as specified by the ratio of the subaperture separation (L_{as}) to the Fried parameter (r_o), and by the photon count per subaperture per short exposure image. The thesis analyzes two different approaches to the STF. In addition to generating STF curves for varying seeing conditions, the signal-to-noise ratio (SNR) for a single sampling of short exposure image and wave front measurements is calculated according to the formula SNR = STF/$\sqrt{\text{var}}$, where var is the variance of the STF. The thesis results indicate the STF is severely degraded by a bias that originates from the estimate of the OTF, which is used in the STF calculation. The problem is found to be increasingly severe for improved wave front sensor sampling (denser wave front measurements) and low photon counts. An attempt is made to characterize non-biased regions of the STF.

Self-referenced speckle holography, single frame signal-to-noise ratio, biased estimator

74

17. SECURITY CLASSIFICATION OF REPORT			
UNCLASSIFIED	UNCLASSIFIED	UNCLASSIFIED	UL

Table of Contents

List of Figures

List of Tables

Abstract

The Speckle Holography technique uses a series of short exposure images and associated wave front sensor measurements to reconstruct astronomical images. The reconstruction technique effectively boosts the amplitude of high spatial frequencies to allow for finer resolution of astronomical objects. A simulation package that calculates the optical transfer function (OTF) of a telescopic system was previously developed for the Phillips Laboratory. This software was modified slightly to provide the Speckle Holography system transfer function (STF) for a telescopic system under varying seeing conditions as specified by the ratio of the subaperture separation (L_{as}) to the Fried parameter (r_o), and by the photon count per subaperture per short exposure image. The thesis analyzes two different approaches to the STF. In addition to generating STF curves for varying seeing conditions, the signal-to-noise ratio (SNR) for a single sampling of short exposure image and wave front measurements is calculated according to the formula:

$$\text{SNR} = \frac{\text{STF}}{\sqrt{\text{var}}},$$

where var is the variance of the STF. The thesis results indicate the STF is severely degraded by a bias that originates from the estimate of the OTF, which is used in the STF calculation. The problem is found to be increasingly severe for improved wave front sensor sampling (denser wave front measurements) and low photon counts. An attempt is made to characterize non-biased regions of the STF.

SELF-REFERENCED SPECKLE HOLOGRAPHY (SRSH) IMAGE RECONSTRUCTION PERFORMANCE

I. Atmospheric Turbulence and the SRSH Technique.

1.1 Introduction.

Prior to the space-based Hubble telescope, ground based telescopes were the only means for observing distant stars. Although a space based telescope has the advantage of not having to "look" through the atmosphere, maintenance costs and size limitations for spaced based systems ensure that ground-based telescopes will continue to remain a vital tool for exploring the universe.

From a diffraction theory perspective, a ground based telescope should be built as large as possible since the larger the telescope diameter, the finer the angular resolution of the telescope and the smaller the object the telescope can image. It turns out that the resolution of large diameter telescopes is limited by the effects of atmospheric turbulence. The turbulence induces random spatial and temporal fluctuations on wave fronts prior to imaging by the telescope, blurring the image and decreasing the angular resolution from the theoretical limit.

Wave front measurements and signal processing can be used to partially overcome the effects of turbulence on images. In this thesis, a FORTRAN computer simulation is used to examine the imaging performance of the self-referenced speckle holography (SRSH) image reconstruction technique. This technique shows great promise, with imaging results approaching the theoretical angular resolution limit of large diameter telescopes to which it is applied [1:1]. In this chapter, the reader is introduced to the problem of imaging through atmospheric turbulence, followed by an introduction to the SRSH technique, and general thesis objectives. In Chapter II, the general theory of the SRSH technique is presented along with assumptions and defining equations for the thesis. The FORTRAN computer simulation is described in some detail in Chapter III. The results for

this thesis effort are presented in Chapter IV and conclusions and recommendations are presented in Chapter V.

1.2 Atmospheric Turbulence.

1.2.1 Turbulent eddies. Atmospheric turbulence is generated by uneven heating and cooling of the earth's atmosphere. This process results in randomly generated pockets of turbulence or eddies, each of which has an index of refraction defined by [2:56]:

$$n = \frac{c}{v}, \tag{1.1}$$

where n is the index of refraction, c (m/s) is the speed of light in a vacuum, and v (m/s) is the velocity of propagation of light in the medium. Each pocket of turbulence can have a different index of refraction from other pockets of turbulence. These pockets occur randomly in a temporal and spatial sense, and so induce random temporal and spatial fluctuations on wave fronts passing through the turbulent region, causing image distortions [3:4527].

Figure 1.1 shows a wave front prior to and after encountering turbulence while enroute to a ground based telescope. Light from a star is essentially planar by the time it reaches the earth's atmosphere due to the distance of propagation. In traveling through the atmosphere to a ground based telescope, the planar wave front encounters the randomly distributed turbulent eddies. The overall delay experienced by a specific point on the wave front will depend on which turbulent eddies that point encounters as it passes through the turbulent atmosphere.

1.2.2 Minimum angular resolution in turbulent conditions. The net effect of this turbulence is to reduce the angular resolution of a large telescope. In theory, the diffraction limited

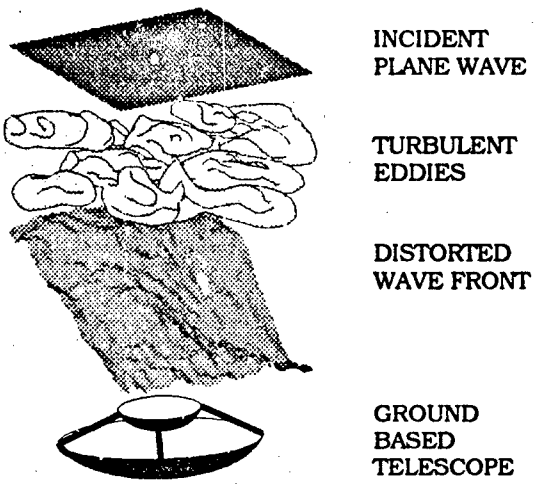

Figure 1.1. Wave front degradation due to atmospheric turbulence.

angular resolution of a telescope is given by [2:422]:

$$\Delta\theta_{\text{min}} = 1.22\frac{\lambda}{D}, \tag{1.2}$$

where $\Delta\theta_{\text{min}}$ (rad) is the angular resolution of the telescope, λ (m) is the wavelength of the incident light, and D (m) is the telescope diameter. Equation (1.2) implies the angular resolution improves with increasing telescope diameter.

Fried derived a parameter in 1966 to describe the point at which increasing atmospheric distortion limits the resolution performance of a telescope [4:33]. The so-called Fried coherence diameter or Fried parameter, r_o, is a measure of the lateral spatial coherence properties of incident wave fronts [5:10–13]. The Fried parameter is roughly on the order of the size of the sloped regions induced on a wave front. The Fried parameter is a function of the wavelength of the light, the propagation path length through the turbulence, the zenith angle (angle with the vertical), and the

strength of the turbulence. If the telescope diameter is less than the Fried parameter, the telescope operates with essentially diffraction limited performance. When the telescope diameter exceeds the Fried parameter (as is generally the case for large diameter telescopes at visible wavelengths), the angular resolution achievable is approximated by replacing D in equation (1.2) by r_o to give [6:14]:

$$\Delta\theta_{\min} = 1.22\frac{\lambda}{r_o}. \tag{1.3}$$

The minimum angular resolution of large diameter ground based telescopes is generally limited to around 1 arcsecond at visible wavelengths [7:1-2]. For example, the 2.4 meter diameter Hubble telescope has a diffraction limit of 0.03 arcsecond in space. On the ground, this same telescope would be limited to angular resolutions on the order of 0.5 to 1.0 arcseconds [6:1,14], which is 16 to 30 times worse than the theoretical limit.

The Fried parameter, r_o, typically ranges from 3 centimeters for poor seeing conditions to 20 or 30 centimeters for good seeing conditions. Its value is site dependent, since the altitude of an observatory site determines how much of the atmosphere the light propagates through. Its value is also weather dependent [6:14]. Typically, atmospheric turbulence limits large diameter telescopes to the same angular resolution as smaller telescopes on the order of 10 to 20 centimeters in diameter.

1.3 Historical Development of the SRSH Technique.

Several image recovery techniques have been developed that involve computer post processing of a series of short exposure images to recover an improved image of the original object. The reason for using short exposure images is, according to Goodman, to "'freeze' the atmospheric degradations, thus eliminating any time averaging effects [8:402]." A long exposure image is blurred by the changing atmospheric conditions causing the image to move around during the exposure. These image changes occur on the order of milliseconds [6]. An example of a long exposure image is shown in Figure 1.2 (a). A short exposure image, see Figure 1.2 (b), contains diffraction limited

spots or speckles. These speckles result "from interference of a signal with itself or with part of the actual imaging or optical system [1:1]." A series of short exposure images can be processed to reconstruct a near diffraction limited image as evidenced by Labeyrie's Speckle Interferometry technique, the Knox-Thompson algorithm technique, and the Triple Correlation technique. All of these image post processing techniques can effectively reconstruct images out to near the diffraction limit of the telescope. The problem with these techniques is they can require thousands of short exposure images [9:64].

An alternative to post processing is what Hardy calls active optics or adaptive optics compensation [10:654]. For this technique, distorted wave fronts are compensated real time by use of a controllable corrective surface whose refractive or reflective properties are changed to cancel the incident wave front distortion. The technique consists of measuring the phase distortion along the wave front and then applying the appropriate controls to the refractive or reflective surface. The three parts to such a system are the controllable corrective surface, wave front sensor device, and information processing device required to generate control signals for the corrective surface.

One type of commonly used wave front sensor device is the Shack-Hartmann wave front sensor (WFS), which has the ideal capability of detecting local wave front slopes at low light levels [1:11]. Figure 1.3 shows an array of subapertures in a Shack-Hartman WFS. The telescope aperture of length D is subdivided into smaller apertures of dimension L. Each of these small apertures, or subapertures, has a lens that focuses that portion of the wave incident on the subaperture onto a detector. The local slope of the incident wave front is sensed separately in the x and y directions by measuring the distance the light is focused off axis as shown in Figure 1.4. The Shack-Hartman WFS provides the key capability of local tilt measurements for the SRSH technique, and its development resulted in practical application of the SRSH technique in image reconstruction.

Fontanella first proposed enhancing post processing image reconstruction performance through a new technique that used simultaneous monochromatic short exposure speckled images and wave

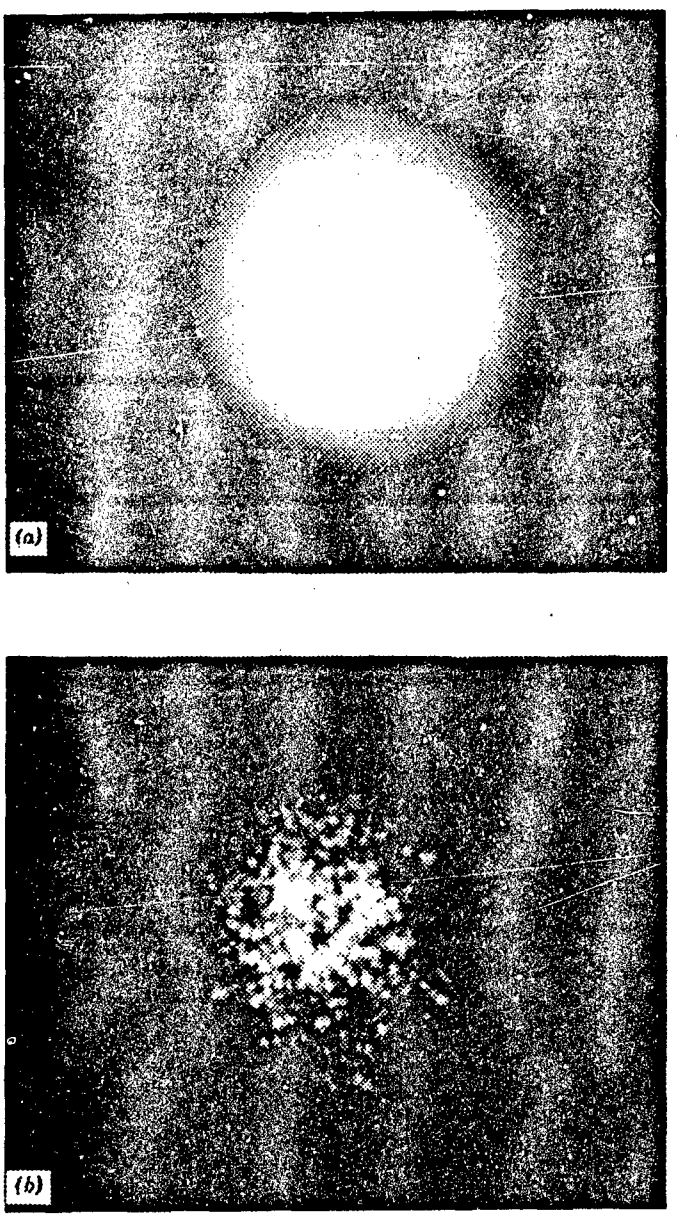

Figure 1.2. Examples of (a) long and (b) short exposure images. [8:403]

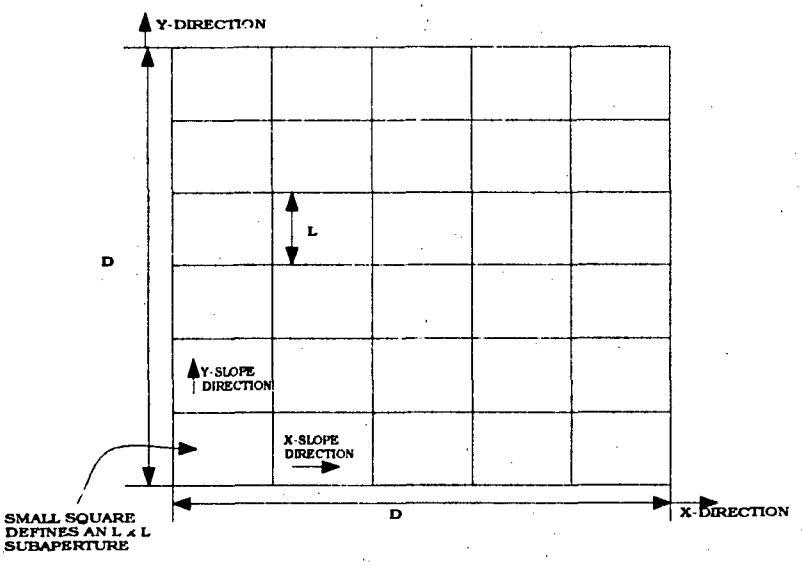

Figure 1.3. Shack–Hartman wave front sensor (WFS) subaperture configuration.

front measurements using the Shack–Hartman sensor [9:64]. This new hybrid approach combined short exposure image post processing with the adaptive optics WFS measurements to remove the effect of the turbulent atmosphere. This technique is called Speckle Holography due to the use of speckled short exposure images such as that shown in Figure 1.2 (b), and the use of a reference wave front (similar to holography recordings) from a point source for phase measurements [11:4527]. The SRSH technique differs only from Speckle Holography in that for the SRSH technique, the object itself acts as its own reference for phase measurements.

1.4 General Thesis Objectives.

This thesis will address the performance of the SRSH technique by first investigating the validity of results from earlier work by VonNiederhausern that characterized the ensemble average Fourier domain system transfer function (STF) for the SRSH technique [16]. The STF is the Fourier domain transfer function for the inversion from the degraded image spectrum to the estimated object spectrum. The SRSH technique removes turbulence degradations in the image by filtering in

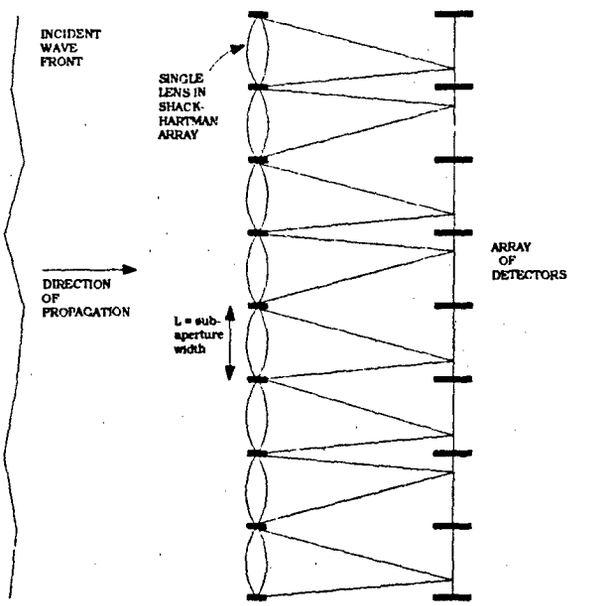

Figure 1.4. Side view of Shack-Hartman wave front sensor (WFS) lens and detector array.

the Fourier domain. The STF results from this earlier work were characterized for variations in the Fried parameter (r_o) and the strength of the incident light (average photon count per subaperture per short exposure image). This thesis uses a FORTRAN simulation to generate STF results by performing calculations on a limited numbers of short exposure images and WFS measurements. This thesis will consider two different approaches to calculating the STF as defined in Chapter II. Additionally, this thesis presents results for a signal to noise ratio (SNR) analysis that characterizes the single frame STF imaging performance as a function of spatial frequency. An unexpected STF bias problem is also investigated and characterized for this thesis.

A discussion of the hardware required, the basic theory of the SRSH technique, and assumptions and defining equations for the thesis appears in the next chapter.

II. General Theory of the SRSH Technique.

2.1 Introduction.

This thesis presents results from a FORTRAN computer simulation of a telescope configured with the hardware shown in Figure 2.1. As background for the SRSH simulation, the basic Fourier theory for a simple lens equivalent model is presented. This simple system configuration is basicly the optical system used by the simulation. Next, the defining equation of the SRSH technique, the system transfer function (STF), is derived using the simple lens model. Finally, the assumptions and defining equations for the thesis are presented.

2.2 Hardware Configuration for the SRSH Technique.

As shown in Figure 2.1, the SRSH technique requires a fast shutter to control exposure times, a beam splitter to split an incident wave front for simultaneous short exposure image and wave front measurements, a wave front sensor for wave front measurements (Shack-Hartman sensor), a filter to pass quasimonochromatic light, a camera for recording the short exposure images, and a computer to construct an estimate of the original object using wave front measurement and short exposure image data [11:4528]. The image is a two dimensional intensity distribution, $i(x, y)$, while the wave front measurements are actually slope measurements that are used to construct an estimate, $\hat{\phi}(x, y)$, of the phase of the incident wave front phase, $\phi(x, y)$. The simulation uses an adaptive optics control law to construct the phase estimate, $\hat{\phi}(x, y)$. An estimate of the object being imaged, $\hat{o}(x, y)$, is obtained by applying the SRSH algorithm over many frames of simultaneous phase estimates and short exposure images.

2.3 Lens Equivalent Model.

For most astronomical scenarios involving large diameter telescopes, and good "seeing" conditions where clouds and other aerosols are not present, the atmospheric distortion induces mainly

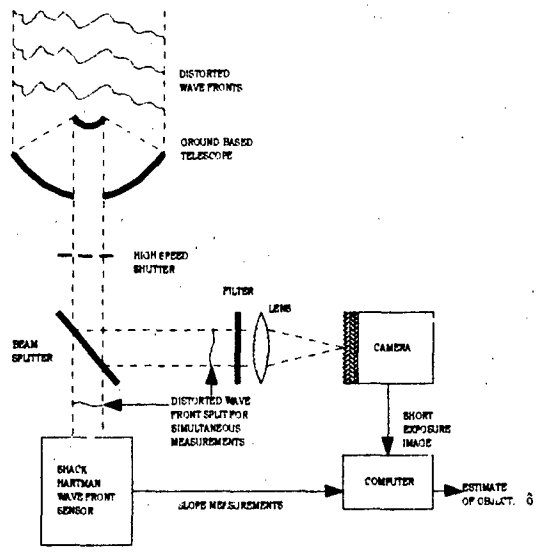

Figure 2.1. Typical SRSH hardware configuration.

phase distortions [8:362]. This result occurs when the turbulence through which the telescope is viewing the object is constrained to what is called the near field. For zenith angles close to zero and a large diameter telescope, one can expect less than a 4 percent error in calculations due to neglecting the amplitude distortions [12:588–589]. The near field assumption holds for the FORTRAN simulation since the telescope diameter is sufficiently large and the zenith angle is zero. So, the turbulent atmosphere for short exposure image formation can be modeled by a single phase screen that introduces delays across the incident wave front [11:4527]. A sample wave front coming from such a phase screen is shown in the greyscale plot (81 by 81 pixels) in Figure 2.2 with bright pixels corresponding to small delays and dark pixels to large delays. Figure 2.3 shows a three-dimensional view of a plane wave prior to and after encountering atmospheric turbulence. Notice that one of the types of phase distortion introduced by the atmosphere is an overall average slope or "tilt" to the wave front.

For the simulation, the telescopic imaging system will be modeled by the simple lens equivalent model shown in Figure 2.4. The object of interest is a star, which is modeled by a point source

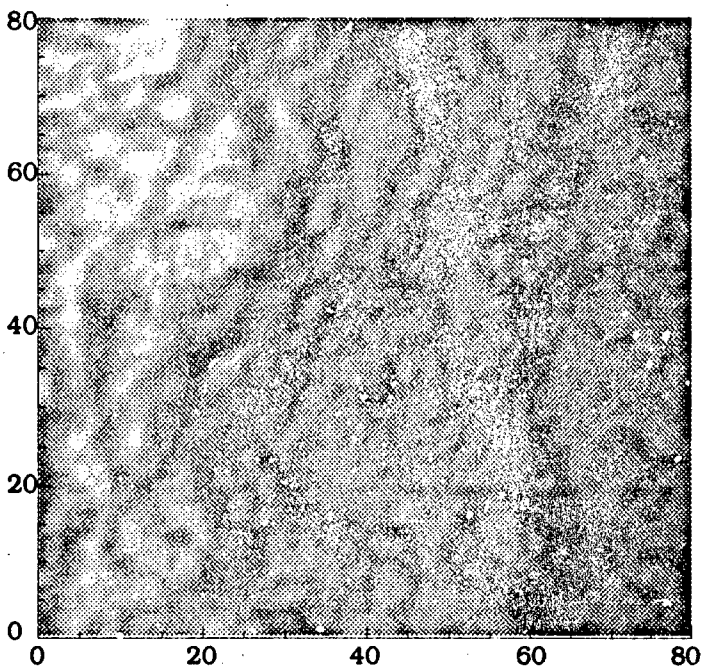

Figure 2.2. Greyscale diagram for wave front encountering turbulence.

at infinite distance away. The atmospheric turbulence is accounted for by a random phase screen, and the telescope by a limiting aperture and imaging lens. The star produces a planar wave front incident on the phase screen. As discussed previously, the phase screen introduces different phase delays along the wave front in the same fashion as would random turbulence to a planar wave front from a star. This degraded wavefront passes through the aperture, and is focused by the lens onto the image plane. For the SRSH hardware shown in Figure 2.1, the wave front sensor is effectively located in the aperture plane where the wave front is sampled prior to imaging.

2.4 System Transform Function (STF).

2.4.1 Spatial domain image formation - instantaneous point spread function (IPSF). The goal is to find an expression for the impulse response of the optical system shown in Figure 2.4. Using Fourier system concepts, the short exposure image can be related to the original object by a

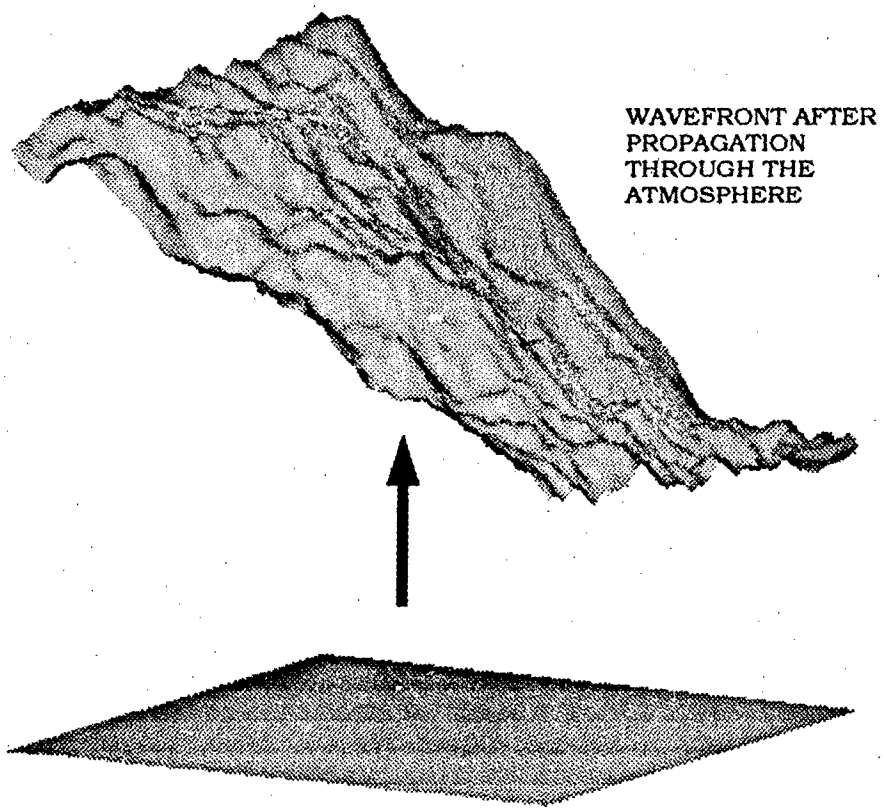

Figure 2.3. Effect on plane wave front encountering turbulence.

convolution relationship:

$$i(\vec{x}) = s(\vec{x}) * o(\vec{x}), \tag{2.1}$$

where $\vec{x}$ is a two–dimensional vector in the image plane, i is the short exposure image, o is the object (star), $*$ stands for a convolution operation, and s is a function called the instantaneous point spread function (IPSF) resulting from the combined effect of the optics and the atmosphere. For a single star in the field-of-view, the IPSF represents the short exposure image.

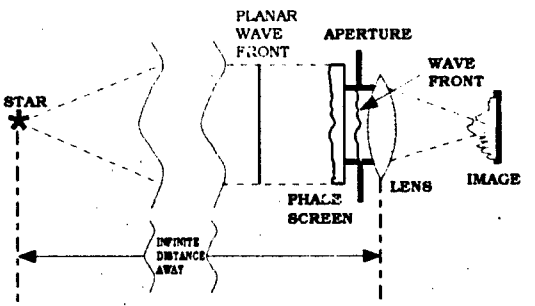

Figure 2.4. Lens equivalent model for telescopic imaging system.

2.4.2 Frequency domain image formation - system transfer function (STF). The convolution relationship in equation (2.1) can be Fourier transformed into the spatial frequency domain to give [11:4527]:

$$I(\vec{\rho}) = S(\vec{\rho})O(\vec{\rho}) \tag{2.2}$$

where I, S, and O are the Fourier transforms of i, s, and o respectively, and $\vec{\rho}$ is the spatial frequency vector. For the case of a star, $o(\vec{x})$ is effectively a point source an infinite distance, and $O(\vec{\rho}) = 1$. This reduces equation (2.2) to:

$$I(\vec{\rho}) = S(\vec{\rho}). \tag{2.3}$$

The function S in equation (2.2), which is known as the optical transfer function (OTF), is determined by the expression [11:4527], [13:113–125]:

$$S(\vec{\rho}) = \frac{[P(\lambda F\vec{\rho})\exp\{j2\pi\phi(\lambda F\vec{\rho})\}] \otimes [P^*(\lambda F\vec{\rho})\exp\{-j2\pi\phi(\lambda F\vec{\rho})\}]}{[P(\lambda F\vec{\rho}) \otimes P^*(\lambda F\vec{\rho})]}, \tag{2.4}$$

where P is the pupil funtion which defines the spatial extent of the aperture of the telescope, ϕ is the wave front phase induced by the phase screen, $*$ indicates the complex conjugate, F is the distance from the pupil plane (aperture in Figure 2.4) to the image plane, and $\otimes$ indicates an autocorrelation operation.

The overall objective of any reconstruction technique is to go from the turbulence degraded image spectrum, I, in equation (2.2), to the best estimate achievable (O) of the original object spectrum, O. An estimate of the original object is then obtained by an inverse fourier transform of this estimated object spectrum. The approach used for the SRSII technique involves using an estimate of the OTF to invert equation (2.2). The problem at hand is to in some way estimate $S(\vec{\rho})$. Since the atmospheric turbulence effects are seen in the wave front phase of the incident wave, wave front sensor measurements are used to estimate the phase in the pupil so that the estimate for the OTF is given by [11:4527]:

$$\hat{S}(\vec{\rho}) = \frac{\left[P(\lambda F\vec{\rho})\exp\{j2\pi\phi(\lambda F\vec{\rho})\}\right] \otimes \left[P^*(\lambda F\vec{\rho})\exp\{-j2\pi\phi(\lambda F\vec{\rho})\}\right]}{[P(\lambda F\vec{\rho}) \otimes P^*(\lambda F\vec{\rho})]}, \tag{2.5}$$

where $\hat{S}$ is the estimate for the OTF, and ϕ is the estimate for the phase screen as determined from the wave front measurements.

Equation (2.2) implies the original object spectrum can be recovered by simply dividing through by the OTF estimate, S. The problem is that $\hat{S}$, as an estimate of S, generally will not contain all the information in S. $\hat{S}$ will most likely contain "zeros" at some spatial frequencies, indicating lost imaging information. A much better approach is to invert equation (2.3) through a Wiener filter type approach so as to minimize the mean square error of the estimate. This estimate of the object spectrum is given as [11:4527]:

$$\hat{O}(\vec{\rho}) = I(\vec{\rho}) \underbrace{\left[\frac{\hat{S}(\vec{\rho})}{|\hat{S}(\vec{\rho})|^2 + \epsilon}\right]}_{\text{Wiener type filter}}, \tag{2.6}$$

where $\hat{O}$ is the estimate of the object spectrum and ϵ is a parametric constant that prevents sigularities in the estimator. Since the single frame OTF estimate, $\hat{S}$, in equation (2.6) will, on average, contain zeros at some spatial frequencies, the estimate of the object spectrum given by equation (2.6) will be incomplete [14:29].

The SRSH approach to image reconstruction is to average a Wiener type filter estimator over many frames so that the estimate of the object spectrum ($\hat{O}$) includes all spatial frequencies out to the diffraction limit of the telescope. There are two possible methods of averaging for the SRSH technique, and both will be considered in this thesis. For the first method considered, the system transfer function (STF) that characterizes the SRSH reconstruction approach, is derived from equation (2.6) by averaging the numerator and denominator to give: [15:2]:

$$STF_1(\vec{\rho}) = \hat{O}(\vec{\rho}) = \frac{\langle S(\vec{\rho})\hat{S}(\vec{\rho})\rangle}{\langle|\hat{S}(\vec{\rho})|^2\rangle}, \tag{2.7}$$

where $STF_1(\vec{\rho})$ represents an ensemble average STF, and the image spectrum $I(\vec{\rho})$ has been replaced by $S(\vec{\rho})$ since, as previously stated, the object is a star. The notation $\langle\cdot\rangle$ represents averaging over an ensemble of a large number of short exposure realizations of $S(\vec{\rho})$ and $\hat{S}(\vec{\rho})$. This equation is used to characterize the performance of the SRSH technique under varying seeing conditions for spatial frequencies out to the diffraction limit of the telescope. Alternately, the STF could be defined by averaging the ratio of numerator and denominator to give:

$$STF_2(\vec{\rho}) = \hat{O}(\vec{\rho}) = \left\langle \frac{S(\vec{\rho})\hat{S}(\vec{\rho})}{\hat{S}(\vec{\rho})\hat{S}^*(\vec{\rho})} \right\rangle, \tag{2.8}$$

where $STF_2(\vec{\rho})$ represents an ensemble average STF.

These two STF estimators, STF_1 and STF_2, represent different approaches to image reconstruction. The magnitude of a STF represents the spatial frequency response of the SRSH technique for the case of a point source object. The results for both SRSH methods are presented in Chapter IV.

2.5 *Assumptions and Defining Equations for the Thesis.*

This thesis is a follow-on to earlier work that involved characterizing the ensemble average performance of the STF_1 algorithm for varying telescope parameters and "seeing" conditions [16]. This thesis uses limited numbers of random phase screens and wave front measurements to estimate the performance of STF_1 and STF_2 algorithms. Additionally, this thesis presents results for STF_1 and STF_2 signal-to-noise ratios (SNRs) that characterize the single frame STF imaging performance as a function of spatial frequency of the two STFs. The assumptions and defining equations for the simulation results are presented in this section.

2.5.1 *Assumptions.*

2.5.1.1 Required sampling. Simulation runs of 2000 frames were assumed sufficient to characterize the performance of the estimator. In general, the SRSH technique requires less frames for image reconstruction.

2.5.1.2 Assumed turbulence characteristics. In modeling the atmospheric turbulence by a phase screen, the assumption is that the amplitude of the incident wave front is not significantly perturbed by the turbulence. This turbulence condition is commonly referred to as near-field turbulence. For astronomical applications, this is a reasonable approximation. The software generated random screens are strictly phase screens and as such do not take into account any amplitude fluctuations.

2.5.2 *Defining equations.*

2.5.2.1 Phase reconstruction. In a practical system, slope measurements are used to reconstruct an estimate of the incident wave front phase $\phi(\vec{x})$ through a linear combination of zonal interpolation functions. For this thesis, the zonal interpolation functions used were two-dimensional

gaussian functions specified by:

$$g_i(\vec{x}) = \exp\left\{\frac{-[\vec{x} - \vec{x}_i]^2}{L_{as}^2}\right\}, \tag{2.9}$$

where g_i is the ith function centered at $\vec{x}_i$, and L_{as} is the radius of the $\frac{1}{e}$ width of g_i. Recall from Figure 1.3 that the wave front sensor divides the aperture up into smaller subapertures over which slope measurements are taken. When reconstructing the wave front from slope measurements, the zonal interpolation functions are located at the corners of the sensors and are weighted appropriately for a best fit of the slope data.

2.5.2.2 Performance related equations and parameters. Both STF_1 and STF_2 and their respective variances were calculated for simulation runs consisting of 2000 frames of simultaneous wave front sensor measurements and short exposure images. The STF results are plotted with respect to a normalized spatial frequency defined by:

$$\vec{\rho}_{\mathrm{n}} = \frac{\vec{\rho}}{\rho_{\mathrm{diff}}}, \tag{2.10}$$

where $\vec{\rho}_{\mathrm{n}}$ is the normalized spatial frequency, $\vec{\rho}$ is the unnormalized spatial frequency, and ρ_{diff} is the magnitude of the maximum or diffraction limited spatial frequency.

An additional way to characterize the STF is through the use of a signal-to-noise ratio (SNR) measure. A single frame SNR is calculated for STF_1 and STF_2 in slightly different fashions. For STF_1, we note that the purpose of the denominator is just to boost the high spatial frequencies. This could be accomplished by a deterministic denominator. All the Fourier phase correction is in the numerator, and so the SNR ratio for STF_1 can be defined by:

$$SNR_1(\vec{\rho}) = \frac{\langle stf_i^{\mathrm{num}}(\vec{\rho})\rangle}{\sqrt{\sigma_{\mathrm{num}}^2(\vec{\rho})}}, \tag{2.11}$$

where SNR_1 is the single frame SNR for STF_1, σ^2_{num} is the variance in the numerator of STF_1, and stf_i^{num} is the ith realization of the numerator of STF_1. For STF_2, the SNR ratio is defined by:

$$SNR_2(\vec{\rho}) = \frac{\langle stf_i(\vec{\rho}) \rangle}{\sqrt{\sigma^2_{stf_i}(\vec{\rho})}}, \tag{2.12}$$

where SNR_2 is the single frame SNR for STF_2 and $\sigma^2_{stf_i}$ is the variance of STF_2.

The SNRs and STFs described above are two dimensional equations. For this thesis, these two dimensional functions are reduced to one dimensional functions for presentation purposes. The reduction is accomplished by angularly averaging as shown in the following reduction of the two-dimensional function $g(\vec{\rho}_n)$ to the single dimensional function $g'(|\vec{\rho}|)$:

$$g'(|\vec{\rho}_n|) = \frac{1}{2\pi}\int_0^{2\pi} g(|\vec{\rho}_n|, \theta) d\theta, \tag{2.13}$$

where $|\vec{\rho}_n|$ and θ are the polar coordinate representation of $\vec{\rho}_n$. These angularly averaged results are presented in Chapter IV.

III. SRSH Computer Simulation.

3.1 Introduction.

The simulation approach to generating SRSH transfer functions STF_1 and STF_2 and their respective SNRs avoids the rather intensive computations required for an analytical approach. In a prior thesis, the analytic derivation of the transfer function STF_1 involved a four dimensional numerical integration [16:3.6]. For the variance calculations required in the SNR analysis, an eight dimensional integration would have to be numerically evaluated.

The SRSH simulation is a modified version of an existing adaptive optics FORTRAN simulation written by Dr. Mike Roggemann while at the Phillips Laboratory, Kirtland AFB, NM. The SRSH simulation uses a least squares phase reconstruction algorithm to produce the phase front estimate $\hat{\phi}$. Additionally, the SRSH simulation uses existing tilt and piston correction, phase screen creation, and OTF calculation algorithms. This chapter first gives a description of simulation steps taken to model a SRSH equiped telescope, and second introduces pertinent analytical equations used in the simulation.

3.2 Simulation of an SRSH Equiped Telescope.

The SRSH technique involves manipulation of the telescope OTF (S) and its estimate ($\hat{S}$) over many frames. The sequence of operations performed by the SRSH simulation to calculate OTFs is shown in Figure 3.1, and will be described in this section. The simulation applies three different templates to the incident wave front ϕ. A WFS template and an associated artificial pupil $P'(\vec{x})$ are used for WFS measurements. This artificial pupil (P') allows for WFS subapertures with corners extending outside the telescope pupil $P(\vec{x})$ to still be used for WFS measurements. The third template is the telescope pupil $P(\vec{x})$ which defines the aperture of the telescope and is used for calculating S and $\hat{S}$. These templates will be described in this section for the sequence of simulation steps required for a single short exposure frame calculation of S and $\hat{S}$.

For a single short exposure frame, the simulation generates a random phase screen or wave front, $\phi(\vec{x})$, incident on the telescope. The next step is to prepare $\phi(\vec{x})$ for wave front sensor(WFS) slope measurements by applying an artificial pupil P' to $\phi(\vec{x})$ prior to application of the WFS sensor template. This is done because the slope in a WFS subaperture is actually determined by sampling wave front $\phi(\vec{x})$ at points along the WFS subaperture edges. As shown in Figure 3.2, the WFS has subaperture corners which extend outside the telescope pupil $P(\vec{x})$. The artificial pupil defines the extent of $\phi(\vec{x})$ for the WFS according to the equation:

$$P'(\vec{x}) = \begin{cases} 1 & \text{if } |\vec{x}| \leq (\frac{D}{2} + \frac{L_{as}}{\sqrt{2}}), \text{ and} \\ 0 & \text{otherwise,} \end{cases} \tag{3.1}$$

where L_{as} defines both the separation between adjacent actuators, and the center-to-center spacing of adjacent subapertures on the WFS.

Since the WFS uses phase differences for slope measurements, it is convenient to remove piston from the incident phase front prior to the WFS measurement. Additionally, the overall tilt can be corrected in the wave front prior to WFS measurements. Tilt is removed only to study possible STF and SNR benefits for tilt correction. The piston and tilt are corrected in the artificial pupil, P', using measurements accross the actual telescope pupil, P, defined by:

$$P(\vec{x}) = \begin{cases} 1 & \text{if } |\vec{x}| \leq \frac{D}{2}, \text{ and} \\ 0 & \text{otherwise,} \end{cases} \tag{3.2}$$

where D is the telescope or aperture diameter. Both pupils are shown in the contour plot in Figure 3.3. This corrected wave front is now used to determine both the OTF and it's estimate by the two separate paths shown in Figure 3.1.

For the OTF estimate ($\hat{S}$), the first step is to apply the wave front sensor template to the corrected wave front. The result, as shown in Figure 3.1, is a wave front sampled along the

defining edges of the wave front sensor subapertures. The reason for this is the simulation uses phase differences across a subaperture to calculate the slope within that subaperture. The wave front sensor template is shown in Figure 3.2, along with the centers of the Gaussian interpolation functions. The estimate of the phase front ϕ is obtained by summing the spatial response of the interpolation functions, each of which is weighted by a factor determined from a linear combination of the slope measurements. The telescope pupil, P, is applied to the phase estimate, and tilt and piston are removed from the phase estimate before calculating S.

For $S(\vec{\rho})$, the first step is to apply the pupil P to the wave front previously corrected for WFS measurements. Next, piston and tilt (if tilt has not been removed prior to the WFS) are removed. The OTF is then calculated from the resulting corrected phase screen. $S(\vec{\rho})$ is actually the frequency domain result of a single frame short exposure image for a single star. Figure 3.4 shows the simulated image plane result. The result is similar to the speckled short exposure image shown in Chapter I.

3.3 Analytical Equations Used in the Simulation.

3.3.1 Flowchart for the SRSH simulation. The SRSH computer simulation follows the flowchart shown in Figure 3.5. The three main sections are Setup, Iterations, and Output. A brief overview of the simulation is presented in this section.

3.3.2 Setup. The first step in the simulation involves specification of arrays and variables, and initialization of simulation parameters. Data is read in to specify the number frames M to process, number of subapertures accross the pupil P, telescope diameter D, Fried parameter r_o, flag for tilt removal (ITILT in Figure 3.5), average photon count per subaperture per exposure N, a small parametric constant to prevent singularities in the STF estimator ϵ, and filenames for simulation output.

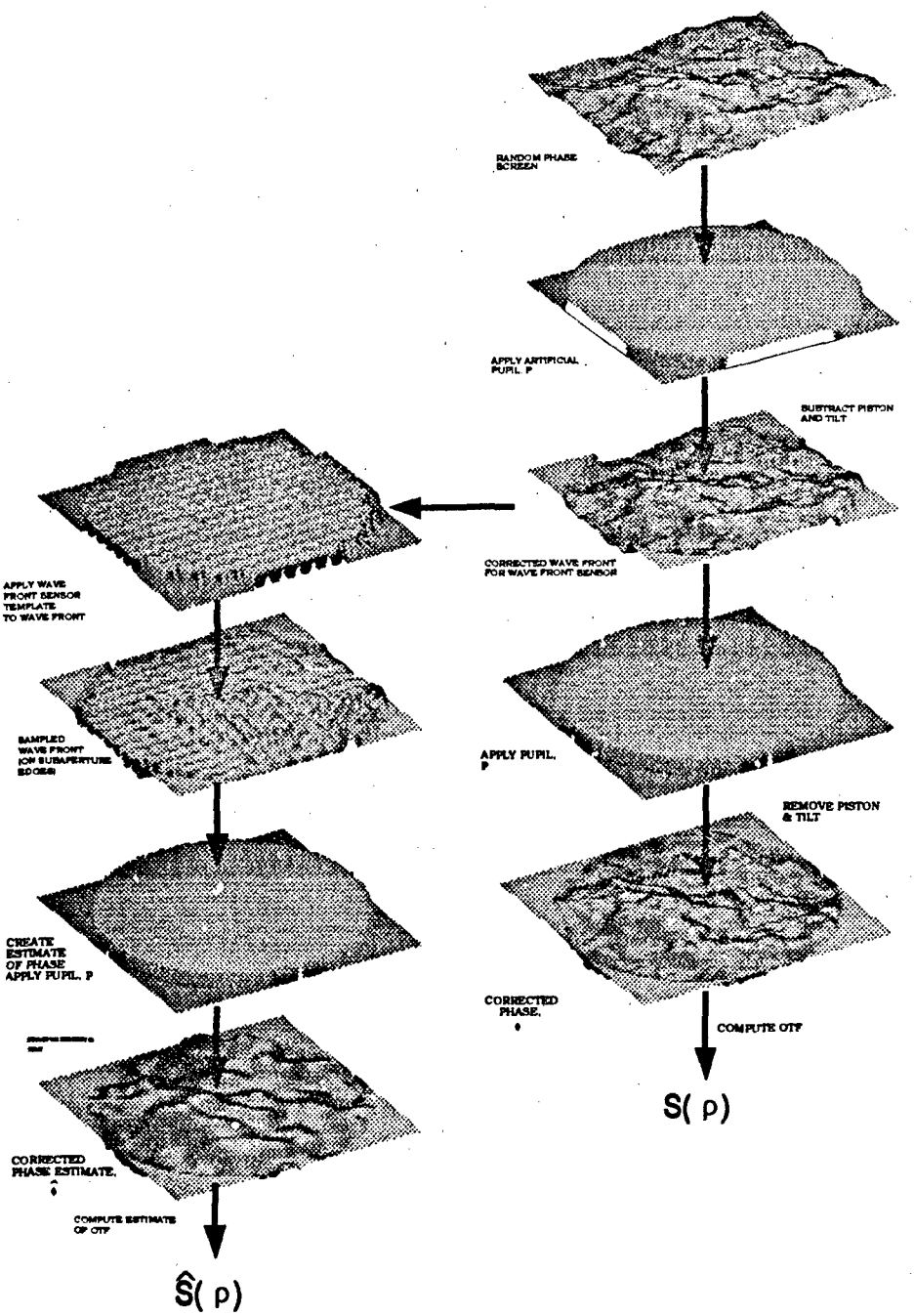

Figure 3.1. Sequence of events for OTF and OTF estimate calculations.

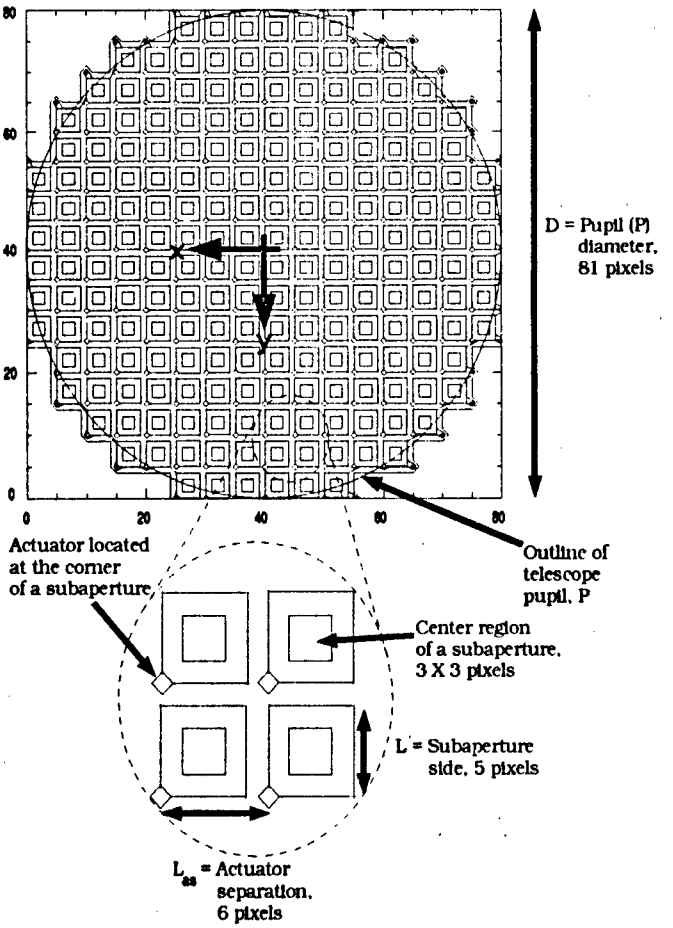

Figure 3.2. Wave front sensor template, with actuator function locations and pupil P shown.

Next, Karhunen-Loève-Fast-Fourier-Transform (KL-FFT) parameters and arrays required for random phase screens are set-up. This method of constructing random phase screens is summarized briefly in Appendix A [17:5]. The phase screen generation is discussed later in the iterations section.

Next, the physical system is specified by creating three template arrays, two of which are the pupil functions, P and P', and the other of which is the Shack-Hartman wave front sensor(WFS). Additionally, gaussian interpolation functions used for the phase estimate are placed in the pupil, with one located at each corner of a subaperture on the wave front sensor. The locations in the

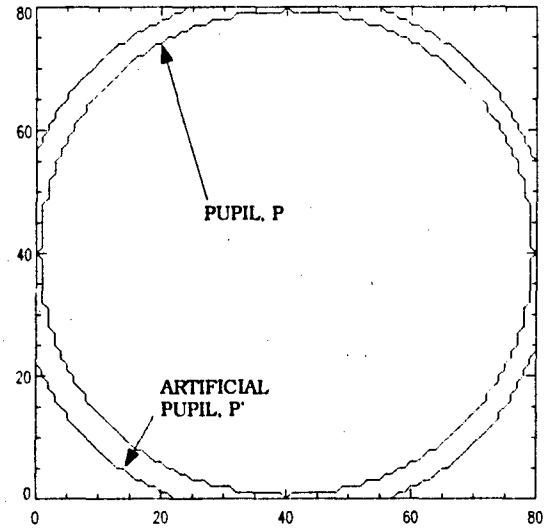

Figure 3.3. Contour plot showing size of actual pupil, P, and artificial pupil, P'.

telescope pupil P for the 208 wave front sensor subapertures and for the centers of the 241 gaussian reconstruction functions are shown in Figure 3.2. Gaussian reconstruction functions are specified by:

$$g_i(\vec{x}) = \exp\left\{-\frac{-[\vec{x}-\vec{x}_i]^2}{L_{as}^2}\right\}, \tag{3.3}$$

where g_i is the ith function centered at $\vec{x}_i$, $\vec{x}$ is the position vector in the pupil, and L_{as} is the distance between adjacent reconstruction functions.

In addition to the WFS used template to model the spatial extent of the subapertures, the simulation also adds in random noise to phase measurements. The accuracy of phase reconstruction is affected by both the signal level in each subaperture of the wave front sensor, and the strength of atmospheric turbulence. Low light levels lead to noisier measurements. Additionally, the Fried parameter, r_o, is a measure of turbulence that relates to the spot size and so must also be considered. By modeling the focused spot of a subaperture lens as gaussian in shape, the standard deviation

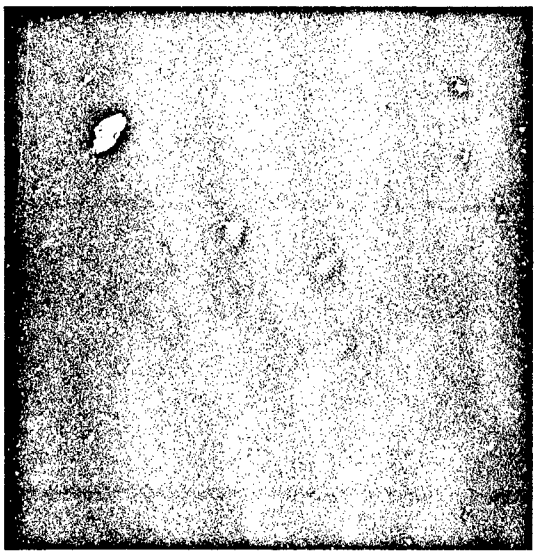

Figure 3.4. Example of simulation short exposure image.

for phase tilt measurements in the x or y directions is given as [18:1919]:

$$\sigma_n = \begin{cases} \frac{0.86\pi\eta}{\sqrt{N}r_o} & L > r_o, \text{ and} \\ \frac{0.74\pi\eta}{\sqrt{NL}} & L \leq r_o, \end{cases} \tag{3.4}$$

where σ_n (rad/m) is the standard deviation of the tilt measurement and η is a dimensionless parameter accounting for imperfections in the subaperture focal plane detector. This standard deviation is used to generate random numbers which are added into phase front measurements as noise.

The final step prior to entering the iterative loop of the simulation is to derive a least-squares reconstruction matrix, R^{ls}, which is used for converting wave front slope measurements into weightings for the phase interpolation functions. The resulting weightings are used to construct a phase estimate by summing the responses of the 241 appropriately scaled Gaussian interpolation

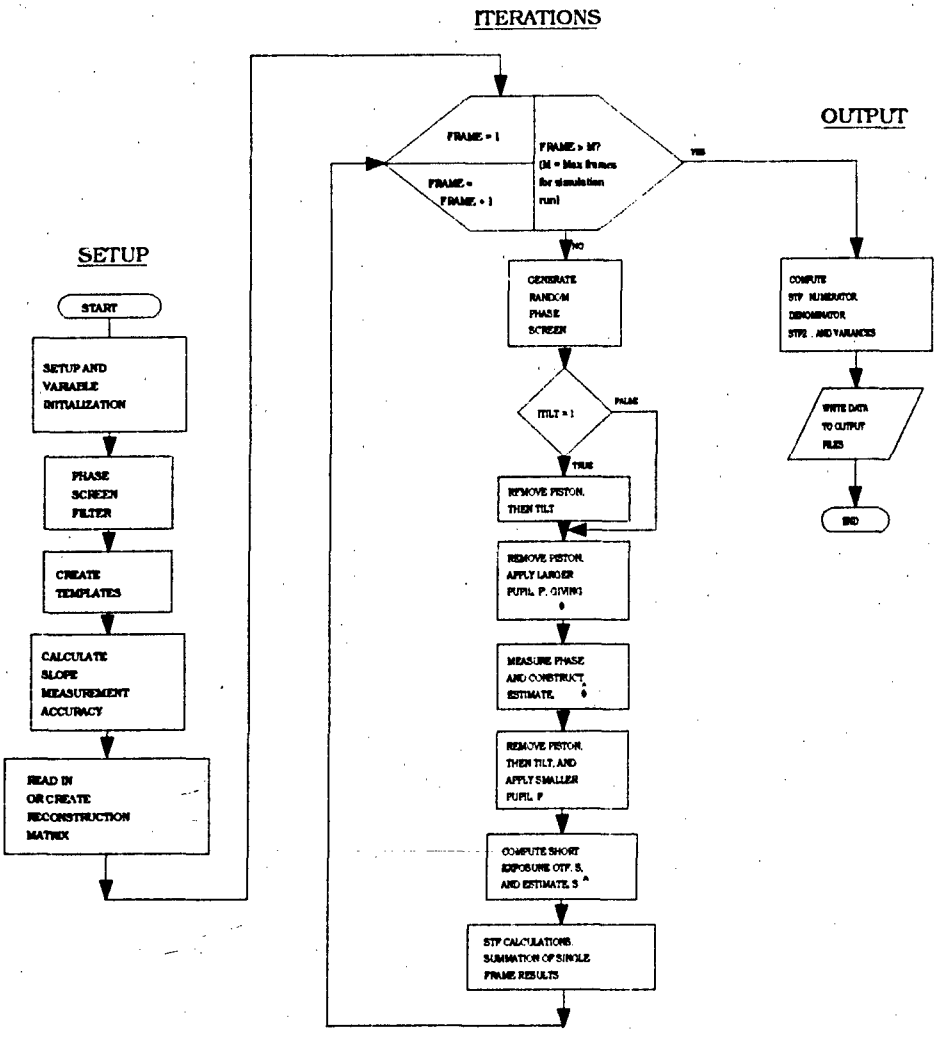

Figure 3.5. Flow chart for the SRSH computer simulation.

functions according to the equation:

$$\phi(\vec{x}) = \sum_{k=1}^{241} c_k g_k(\vec{x}) \tag{3.5}$$

where g_k is the kth numbered Gaussian interpolation function located at a corner of a subaperture, and c_k is its associated weighting. The least squares approach is used to solve for the required weighting factors by inverting the linear equation:

$$\mathcal{S} = HC, \tag{3.6}$$

where C is a vector containing the required weightings (c_k), $\mathcal{S}$ is a vector containing slope measurements ($s_i^{x \text{ or } y}$), and H is a Jacobian matrix whose elements are defined by $\frac{\delta s_i}{\delta c_k}$ [19:457–458] [20:19–20]. For the particular geometry considered here, 241 weightings are determined from 416 slope measurements. The linear system described by equation (3.6) is what Tyson describes as "overdetermined [4:237]," having fewer unknowns (required weightings) than linear equations to solve. A "best fit" to the data (slope measurements) that minimizes the mean square error between the left and right sides of equation (3.6) gives the required weightings as:

$$C = \underbrace{(H^T H)^{-1} H^T}_{R^{ls}} \mathcal{S}, \tag{3.7}$$

where R^{ls} is defined as the least squares reconstruction matrix used to map slope measurements into actuator commands for phase estimate construction.

3.3.3 Iterations. The simulation produces results for M short exposure frames. Each pass of the iteration loop involves phase screen generation, tilt and piston correction, phase estimation, S and $\hat{S}$ calculations, and summation of STF results with those from previous frames.

3.3.3.1 Phase screen generation. The KL-FFT technique is used to generate random phase screens. The technique involves the creation of an FFT screen by the inverse transform of appropriately filtered complex Gaussian random variables. This FFT sceen is corrected by two low order KL functions, producing the complex KL-FFT screen $\tilde{\Psi}_{fft-kl}$, which is scaled for the turbulence strength (multiply by $\left[\frac{D}{r_o}\right]^{\frac{5}{6}}$). The random phase screen ϕ is taken from the real or imaginary part of $\tilde{\Psi}_{fft-kl}$. The real part is used on odd and the imaginary part on even numbered frames. The details of this technique are discussed in Appendix A.

3.3.3.2 Tilt and piston correction. Next, the piston error of the random phase screen, ϕ, is measured in the telescope pupil, P, and removed over the larger pupil, P', as follows [15:3–4]:

$$\phi'(\vec{x}) = \left[\phi(\vec{x}) - \int d^2\vec{x} P(\vec{x})\phi(\vec{x})\right] P'(\vec{x}), \tag{3.8}$$

where ϕ' is the piston corrected wave front. For no-tilt simulations, the tilt in x and y directions is calculated over the pupil P as follows [21:253–255]:

$$t_n = \frac{\int d^2\vec{x}\{\vec{d}_n \cdot \vec{x}\}\phi(\vec{x})P(\vec{x})}{\int d^2\vec{x}\{\vec{d}_n \cdot \vec{x}\}^2 P(\vec{x})}, \tag{3.9}$$

where t_n is the tilt, $\vec{d}_n$ is a unit vector in the x or y direction. In preparation for wave front sensor measurements, the tilt is removed over P':

$$\phi''(\vec{x}) = \left\{\phi'(\vec{x}) - [t_x(\vec{i}\cdot\vec{x}) + t_y(\vec{j}\cdot\vec{x})]\right\} P'(\vec{x}), \tag{3.10}$$

where ϕ'' is the tilt corrected wave front, t_x and t_y are tilts, and $\vec{i}$ and $\vec{j}$ are unit vectors in the x and y directions.

3.3.3.3 Phase reconstruction. Since most of the results for this thesis are for the case of tilt correction prior to WFS measurements, the remaining simulation description will be

for the tilt corrected wave front, ϕ''. Slope measurements are now made on the wave front, ϕ'', by applying the wave front sensor template. For the nth subaperture, the measured slope is given by [18:1914]:

$$s_n = \int d^2\vec{x} W_n(\vec{x})[\nabla\phi''(\vec{x}) \cdot \vec{d}_n] + \alpha_n, \tag{3.11}$$

where $\cdot$ indicates a dot product, s_n is the slope measurement (radians per meter), ∇ is the two-dimensional spatial gradient, $\vec{d}_n$ is a unit vector in the direction of the sensitivity (x or y) of the nth sensor, and α_n is the slope measurement error in radians per meter. Additionally, W_n (units of m^{-1}) is defined as a weighting function for the nth subaperture such that:

$$W_n(\vec{x}) = \int d^2\vec{x} W_n(\vec{x}) = 1. \tag{3.12}$$

The slope is calculated in the simulation from a slightly modified version of equation (3.11) that expresses the integral in in terms of phase differences along the edges of a particular subaperture.

To get the phase difference version for slope, equation (3.11) is first rewritten using integration by parts to give [18:1914]:

$$s_n = -\int d^2\vec{x}\phi''(\vec{x})[\nabla W_n(\vec{x}) \cdot \vec{d}_n] + \alpha_n, \tag{3.13}$$

where the integral is now expressed in terms of the gradient of the weighting function for the nth subaperture, $\nabla W_n(\vec{x})$. For the subaperture shown in Figure 3.6, this gradient can be expressed as:

$$\nabla W_n(\vec{x}) = \overbrace{\int_{x_l}^{x_r} dx\{W_n(x,y_l)\delta(x,y-y_l) - W_n(x,y_r)\delta(x,y-y_r)\} + \underbrace{\int_{y_r}^{y_l} dy\{W_n(x_r,y)\delta(x-x_r,y) - W_n(x_l,y)\delta(x-x_l,y)\}}_{\text{used to calculate slope in } x \text{ direction}}}^{\text{used to calculate slope in } y \text{ direction}}, \tag{3.14}$$

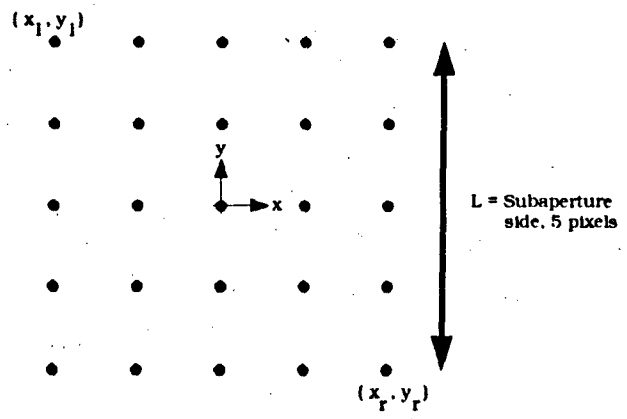

Figure 3.6. Location of points on nth subaperture.

where $\delta(x, y)$ is an impulse function, and (x_l, y_l) is the coordinate of the upper left corner and (x_r, y_r) the lower right corner of the nth subaperture as shown in Figure 3.6. Using the "sifting" property of an impulse function [22:56–57] equation (3.13) can be rewritten in terms of line integral phase differences along the subaperture edge. For example, the y slope for the nth subaperture is given by:

$$s_n^y = \int_{x_l}^{x_r} dx\, \phi''(x, y_l) W_n(x, y_l) - \int_{x_l}^{x_r} dx\, \phi(x, y_r) W_n(x, y_r) + \alpha_n^y, \tag{3.15}$$

where s_n^y is the y slope for the nth subaperture, and α_n^y is a the additive random noise term of zero mean and standard deviation determined by Equation (3.4).

The reconstruction matrix, R^{ls}, is used to map the vector of slope measurements onto weighting commands for phase reconstruction. The vector of weighting commands is determined by:

$$\mathcal{C} = R^{ls} \mathcal{S}, \tag{3.16}$$

where $\mathcal{C}$ is the vector containing 241 actuator commands for scaling 241 gaussian functions, $\mathcal{S}$ is the vector containing x and y slope measurements (416, two measurements for each of 208 subapertures), and R^{ls} is the reconstruction matrix (241 rows by $2 \times 208 = 416$ columns). The

phase estimate is then constructed by summing the scaled gaussian function responses at each point in the pupil to give:

$$\hat{\phi}(\vec{x}) = \sum_{k=1}^{241} c_k \exp\left\{\frac{-[\vec{x} - \vec{x}_i]^2}{L_{as}^2}\right\} \tag{3.17}$$

where $\hat{\phi}$ is the phase estimate, c_k is the kth weighting command or scaling for the kth gaussian function located at $\vec{x}_i$.

3.3.3.4 Calculating centered OTFs for S and $\hat{S}$. For the SRSH technique, the simulation calculates centered OTFs for S and $\hat{S}$. Centering the OTF is accomplished by removing tilt from the phase fronts. Since this discussion is for tilt removed prior to WFS measurements, ϕ'' is the corrected wave front for calculating S, and as such already has tilt removed. For $\hat{S}$, the phase estimate $\hat{\phi}$ does require tilt correction. Additionally,the telescope pupil P is applied to ϕ'' and $\hat{\phi}$ in preparation for OTF calculations.

$S(\vec{\rho})$ is calculated directly from a forward Fourier transform of the magnitude squared of the coherent impulse response [13:114]:

$$S_i(\vec{\rho}) = \frac{\mathcal{F}\{|h_i(\vec{x})|^2\}}{\mathcal{F}\{|h_i(\vec{x})|^2\}|_{\vec{\rho}=0}}, \tag{3.18}$$

where $\mathcal{F}\{\cdot\}$ indicates a forward Fourier transform, and h_i is the coherent impulse response for the ith frame as defined by [13:111]:

$$h_i(\vec{x}) = \mathcal{F}\left\{P(\lambda F\vec{\rho}) \exp\left\{-2\pi\phi_i''(\lambda F\vec{\rho})\right\}\right\}, \tag{3.19}$$

where λ is the wavelength, and F is the telescope focal length. The estimate of the OTF, $\hat{S}_i$, is obtained if $\hat{\phi}_i$ is used instead of ϕ_i'' in equation (3.19).

Next, STF quantities are calculated. For STF_1, the single frame numerator and denominator are calculated by:

$$stf_i^{\text{num}}(\vec{\rho}) = S_i(\vec{\rho})\hat{S}_i^*(\vec{\rho}), \tag{3.20}$$

and:

$$stf_i^{\text{den}}(\vec{\rho}) = |\hat{S}_i(\vec{\rho})|^2 + \epsilon, \tag{3.21}$$

where ϵ is an arbitrarily small number to prevent divide by zero, stf_i^{num} is the ith frame numerator, and stf_i^{den} is the ith frame denominator. For STF_2, the single frame result is calculated as:

$$stf_i(\vec{\rho}) = \frac{stf_i^{\text{num}}(\vec{\rho})}{stf_i^{\text{den}}(\vec{\rho})}, \tag{3.22}$$

where stf_i is ith frame result.

3.3.4 Results of simulation run. The STF's are calculated by averaging the single frames results over M frames. So, $STF1$ is calculated as follows:

$$STF_1(\vec{\rho}) = \frac{\langle stf_i^{\text{num}}(\vec{\rho})\rangle}{\left\langle stf_i^{\text{den}}(\vec{\rho})\right\rangle}. \tag{3.23}$$

Finally, $STF2$ is found by:

$$STF2(\vec{\rho}) = \langle stf_i(\vec{\rho})\rangle, \tag{3.24}$$

where $stf_i(\vec{\rho})$ is the ith single frame result.

The SNR for a single frame of the image can be defined in the spatial frequency domain as [19:452]:

$$SNR(\vec{\rho}) = \frac{\langle I(\vec{\rho})\rangle}{\sqrt{\sigma_I^2(\vec{\rho})}}, \tag{3.25}$$

where I is the Fourier transform of the image and $\sigma_I^2(\vec{\rho})$ is the image variance. For SNR calculations, the variance is calculated for functions according to the equation [23:244]:

$$\sigma_f^2(\vec{\rho}) = \left\langle [f_i(\vec{\rho})]^2 \right\rangle - \left\langle f_i(\vec{\rho}) \right\rangle^2 , \tag{3.26}$$

where $\sigma_f^2(\vec{\rho})$ is the variance of the random process $f(\vec{\rho})$, and $f_i(\vec{\rho})$ is ith frame realization of the function. Instead of an image, this thesis is interested in the SNR of the STF estimators. For STF_1, the SNR is defined in terms of the complex numerator, stf_i^{num}. The single frame SNR for STF_1 is defined by:

$$SNR_1(\vec{\rho}) = \frac{\langle stf_i^{\text{num}}(\vec{\rho}) \rangle}{\sqrt{\sigma_{\text{num}}^2(\vec{\rho})}}, \tag{3.27}$$

where $\sigma_{\text{num}}^2(\vec{\rho})$ is the variance of the $STF_1(\vec{\rho})$ numerator. For STF_2, the single frame SNR is defined in a more straightforward fashion as:

$$SNR_2(\vec{\rho}) = \frac{\langle stf_i(\vec{\rho}) \rangle_M}{\sqrt{\sigma_{stf_i}^2(\vec{\rho})}}, \tag{3.28}$$

where $\sigma_{stf_i}^2(\vec{\rho})$ is the variance of $stf_i(\vec{\rho})$. The results for SNRs and STFs are presented in the next chapter.

IV. Simulation Results.

4.1 Introduction.

This chapter presents simulation results of the system transfer function (STF) and associated signal-to-noise ratio (SNR) measures defined in Chapter II. This chapter will begin with a review of previous analytic results for the SRSH technique found in Reference [24]. These analytic results characterize the STF, and as such, serve as the basis for this thesis effort. General analytic STF trends will be used for discussing the validity of simulation STF results.

Next, STF_1 and STF_2 results are presented. The simulation results were generated using 2000 randomly generated phase screens and the conditions summarized in Table 4.1. The telescope diameter (D) was set at two meters. Also, the parametric constant (ϵ) to prevent divide by zero in STF calculations was set at 1×10^{-9}. Only selected results from these runs are presented in this thesis. Individual STF simulation runs are characterized by a subaperture light level (average photons per subaperture per short exposure image, N), possibility of tilt correction, and ratio of center-to-center subaperture separation to Fried parameter, $\frac{L_{ss}}{r_o}$. This ratio, $\frac{L_{ss}}{r_o}$, defines the adequacy of the wave front sampling in detecting the turbulence characteristics of the incident wave front. Although correcting tilt prior to the WFS is optional, the majority of the results discussed will be for the case of tilt corrected phase fronts. Not removing tilt leads to a higher error in the phase estimate. The effect of no-tilt removal will be briefly examined for STF_1.

This chapter also presents an analysis of the non-zero mean bias terms in the numerator and denominator of the STF. The results indicate the OTF estimate, $\hat{S}$, contains a negative bias. The bias problem is particularly significant under the combined conditions of low incident light levels and good WFS sampling (sampling ratio $\frac{L_{ss}}{r_o}$ less than one).

The final simulation results presented are selected frequency domain SNRs which characterize, as a function of spatial frequency, the single frame STF image reconstruction performance. The SNRs can be used to determine the number of short exposure frames of data to obtain a required

PARAMETER	VALUES USED
PHOTONS PER SUBAPERTURE PER SHORT EXPOSURE IMAGE	10, 20, 50, 100, 200, 400, 800, 1000
RATIO OF SUBAPERTURE SIZE TO FRIED PARAMETER, L/r_0	0.25, 0.5, 1.0, 2.0
PHASE CORRECTIONS PRIOR TO WAVE FRONT SENSOR	NONE, OR CORRECT TILT
CONTROL LAW USED FOR CONSTRUCTING ESTIMATE OF THE PHASE	MINIMUM MEAN SQUARE ERROR

Table 4.1. Scenarios considered for thesis research.

SNR level out to a given spatial frequency. The analytic consideration of Reference [24] did not include any SNR results due to the required eight-dimensional numeric integration for the STF variance. The ratio $\frac{SNR_1}{SNR_2}$ is presented to discuss the comparative advantages of STF_1 and STF_2.

4.2 Summary of Previous Analytic Results [24:15-16].

The analytic results presented in this section are for a numeric integration of a derived four dimensional integral expression for the STF in terms of the OTF (S) and its estimate ($\hat{S}$) [24:10]. Due to the complexity of this integration, the analytic results are for case of a simple square aperture telescope and a small number of WFS subapertures. The WFS used has a maximum of five subapertures accross the telescope pupil as shown in Figure 4.1. Analytic results are presented for variations in both the average photon count per subaperture per short exposure image N, and the WFS sampling ratio, $\frac{L_{ss}}{r_o}$. Analytic result trends are used for discussing the validity of simulation STF results in the next section. The comparison is not rigorous since analytic STF results are for a different phase estimate construction control law (minimum variance), and are for a square telescope pupil.

The analytic STF is characterized for variations in the both the the average photon count per subaperture per short exposure image (N) and the sampling ratio ($\frac{L_{as}}{r_o}$). In general, WFS measurements improve with increasing signal strength of the incident light as specified by increasing N. The other important parameter concerns how dense the WFS measurements are compared to the Fried parameter r_o. The slopes are measured in WFS subapertures with center-to-center spacings of L_{as}. The ratio of $\frac{L_{as}}{r_o}$ is used to compare the slope measurement spacing to the turbulence conditions indicated by the Fried parameter. Smaller $\frac{L_{as}}{r_o}$ values signify more dense WFS measurements with respect to the size of turbulence induced distortions on the incident wave front since r_o characterizes the approximate size of significant wave front distortions. If the sampling ratio is less than unity, most of the turbulence characteristics along the incident wave front are being accurately measured since L_{as} is smaller than r_o. Poor sampling is characterized by sampling ratios greater than unity. For the analytic results, N ranges from 10 to 400, and $\frac{L_{as}}{r_o}$ from 0.1 to 2.

The analytic results, which are from a paper by VonNiederhausen and Welsh, are summarized in Figures 4.2 and 4.3 [24:15-16]. The STF results are plotted versus a one-dimensional normalized spatial frequency, $\frac{f_x \lambda F}{D}$, where f_x represents the x-component of the two-dimensional spatial frequency vector $\vec{\rho}$, and F is the focal length of the telescope.

The STF is a measure of the spatial frequency response of the SRSH reconstruction technique. Ideally, the STF would be unity out to the diffraction limit of the telescope. For a sampling ratio of unity, Figure 4.2 shows how the SRSH technique performance improves toward ideal behavior with increasing light intensity (N increases). The curves asymptotically approach an upper limit imposed by the sampling ratio.

Figure 4.3 illustrates the positive result on STF performance obtained by decreasing the sampling ratio. For these results, the average photon count is held at $N = 50$, while the sampling ratio ranges from 0.1 to 2. The STF curves indicate that the technique is extremely sensitive to the sampling ratio.

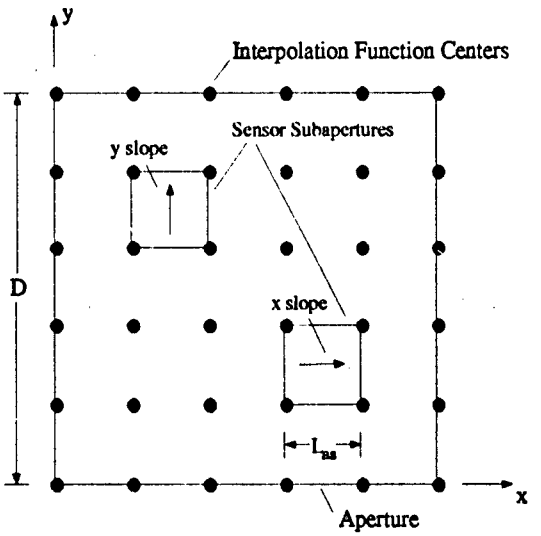

Figure 4.1. Telescope aperture and wave front sensor geometry for analytic results [24:13].

In summary, both light intensity level (N) and sampling ratio ($\frac{L_{sa}}{r_o}$) are important parameters for characterizing expected STF image estimator performance. The simulation STF behavior will now be examined for variations in these two parameters.

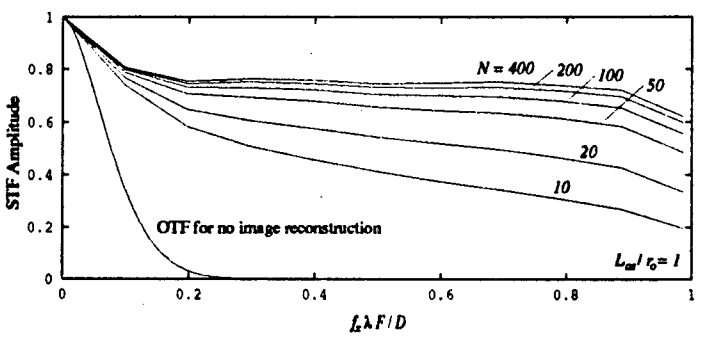

Figure 4.2. System transfer function (STF) results for square aperture and WFS shown in Figure 4.1 and $\frac{L_{sa}}{r_o} = 1$ [24:15].

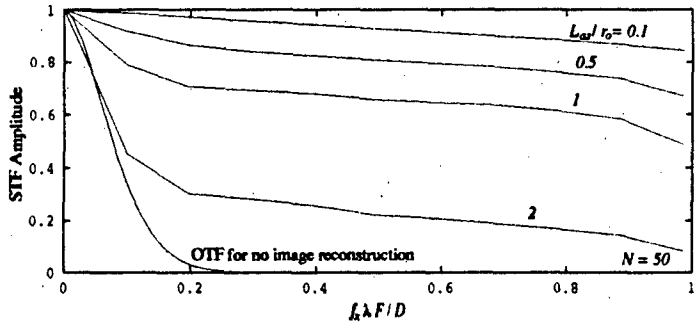

Figure 4.3. System transfer function (STF) results for square aperture and WFS shown in Figure 4.1 and $N = 50$ [24:16].

4.3 STF Results.

The simulation STF results will be examined in terms of the general trends noted for the analytic STF results in the previous section [16:4.8-4.15]. Specifically, STF curves should approach asymptotic behavior with increasing photon count. This asymptotic value must be equal to or less than unity. The STF curves should also improve with an improved sampling ratio, again approaching but not exceeding unity. Deviations from the trends established by the analytic results will be explained in the next section which investigates a negative noise bias problem originating with the OTF estimate, $\hat{S}$. This section presents a summary of STF results for the case of tilt removed prior to WFS measurements. This is the baseline case for this thesis. To examine the benefit of tilt removal, STF_1 results for tilt removed and tilt not removed are presented for a photon count of 100, and sampling ratios varying from 0.25 to 2.

Figures 4.4 and 4.5 show the tilt removed STF curves for photon counts of 10 and 800, with sampling ratios varying from 0.25 to 2. STF_1 and STF_2 are characterized by non-zero valued image reconstruction out to the diffraction limit of the telescope for all sampling conditions considered. Except for a sampling ratio of 0.25, both STF_1 and STF_2 show improved performance for increasing the photon count while holding the sampling ratio fixed. Improving the sampling ratio also generally improves the STF.

The problem with the simulation results is that both STF_1 and STF_2 curves exceed unity at some point for most photon counts and all sampling ratios considered. This deviation from the previously predicted results [24] is due to a non-zero bias in the OTF estimate $\hat{S}$. The bias appears to get worse as the sampling varies from poor ($\frac{L_{as}}{r_o} > 1.0$) to good ($\frac{L_{as}}{r_o} < 1.0$) for both STF estimator methods. For each sampling ratio, the problem gets successively worst for decreasing photon counts, indicating the $\hat{S}$ bias is increased with increased noise in the slope measurements since the standard deviation of the additive noise in slope measurements is proportional to $\frac{1}{\sqrt{N}}$. The best example of this trend is shown in Figures 4.4 and 4.5 for a sampling ratio of $\frac{L_{as}}{r_o} = 0.25$, where the STF curve for the low photon count of 10 stays well above unity, except for spatial frequencies out near the diffraction limit ($\rho_n \Rightarrow 1$). The STF curve for the high photon count of 800 is closer to unity for out to the diffraction limit. These results imply the spatial frequencies of the image are being amplified to give better than the theoretical maximum. This is clearly an unphysical result which has not been previously noted in the literature. The next section traces this result to the bias in $\hat{S}$. The bias is shown to get progressively worse as sampling improves (smaller sampling ratio) and the photon count remains low.

Figure 4.6 shows the effect tilt removal has on STF_1 for a photon count of 100, and varying sampling conditions. At unity and low sampling ratios, removing tilt prior to the WFS boosts the STF_1 estimator curves slightly in magnitude. This effect is most noticeable at spatial frequencies near the diffraction limit. As WFS sampling is improved (sampling ratio drops below one), removing tilt gives some improvement at higher spatial frequencies, with negligible results at lower spatial frequencies.

4.4 Noise characteristics of the simulation STF estimator.

The goal of this section is to characterize the bias terms in the STF. To investigate the problem, the single frame OTF (S) is expressed as a random complex quantity and the OTF

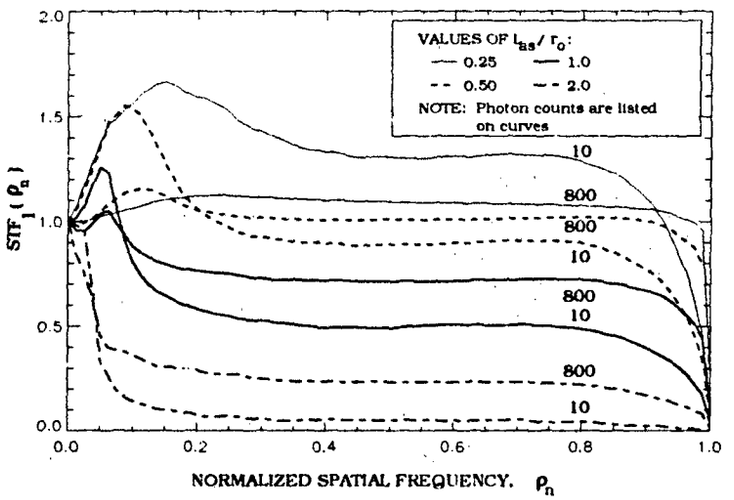

Figure 4.4. Tilt removed STF_1 curves for different wave front sampling conditions as specified by $\frac{L_{as}}{r_o}$.

estimate ($\hat{S}$) as noisy version of S. The noise, $\tilde{\mathcal{N}}$, is then determined from the difference between $\hat{S}$ and S ($\hat{S} - S = \tilde{\mathcal{N}}$). The complex expressions for S and $\hat{S}$ are used to derive expressions for the numerator and denominator of the STF estimator. An investigation of the noise terms in both the numerator and denominator shows the source of the problem is the negative mean of the real part of $\tilde{\mathcal{N}}$ in $\hat{S}$. An attempt will be made to identify, from the bias results, spatial frequency ranges which yield valid simulation STF results (small bias regions).

The first goal of this analysis is to isolate the complex valued additive noise term contained in $\hat{S}$. To do this, S is first expressed as a complex quantity:

$$S(\vec{\rho}) = S_{\mathcal{R}e}(\vec{\rho}) + jS_{\mathcal{I}m}(\vec{\rho}), \tag{4.1}$$

where $S_{\mathcal{R}e}$ and $S_{\mathcal{I}m}$ are the real and imaginary parts of the S, and j indicates the imaginary part. An expression for $\hat{S}$ is found by adding real and imaginary noise components to S in equation (4.1) to give:

$$\hat{S}(\vec{\rho}) = S_{\mathcal{R}e}(\vec{\rho}) + \mathcal{N}_{\mathcal{R}e}(\vec{\rho}) + j\left\{S_{\mathcal{I}m}(\vec{\rho}) + \mathcal{N}_{\mathcal{I}m}(\vec{\rho})\right\}, \tag{4.2}$$

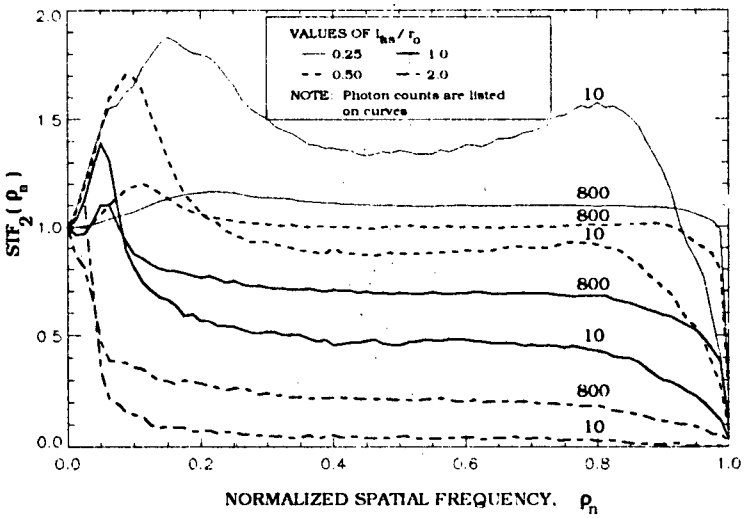

Figure 4.5. Tilt removed STF_2 curves for different wave front sampling conditions as specified by $\frac{L_{sa}}{r_o}$.

where $\mathcal{N}_{\mathcal{R}e}$ and $\mathcal{N}_{\mathcal{I}m}$ are the real and imaginary parts of the additive noise in $\hat{S}$. To isolate the noise in $\hat{S}$, equation (4.1) is subtracted from equation (4.2) to give:

$$\hat{S}(\vec{\rho}) - S(\vec{\rho}) = \mathcal{N}_{\mathcal{R}e}(\vec{\rho}) + j\mathcal{N}_{\mathcal{I}m}(\vec{\rho}) = \tilde{\mathcal{N}}(\vec{\rho}) \tag{4.3}$$

where $\tilde{\mathcal{N}}$ is the complex noise portion of $\hat{S}$. The bias problem originates from a negative mean real noise term in $\tilde{\mathcal{N}}$:

$$\langle \tilde{\mathcal{N}}(\vec{\rho}) \rangle = \langle \mathcal{N}_{\mathcal{R}e}(\vec{\rho}) \rangle < 0, \tag{4.4}$$

with the imaginary noise part, $\mathcal{N}_{\mathcal{I}m}$, having zero mean.

The next step in the noise analysis is to derive complex expressions for the numerator ($S\hat{S}^*$) and denominator ($|\hat{S}|^2$) terms of the STF, and average the expressions to determine significant noise terms. The complex numerator is expressed as:

$$S(\vec{\rho})\hat{S}^*(\vec{\rho}) \quad = \quad S^2_{\mathcal{R}e}(\vec{\rho}) + S_{\mathcal{R}e}(\vec{\rho})\mathcal{N}_{\mathcal{R}e}(\vec{\rho}) + S_{\mathcal{I}m}(\vec{\rho})\mathcal{N}_{\mathcal{I}m}(\vec{\rho}) + S^2_{\mathcal{I}m}(\vec{\rho})$$

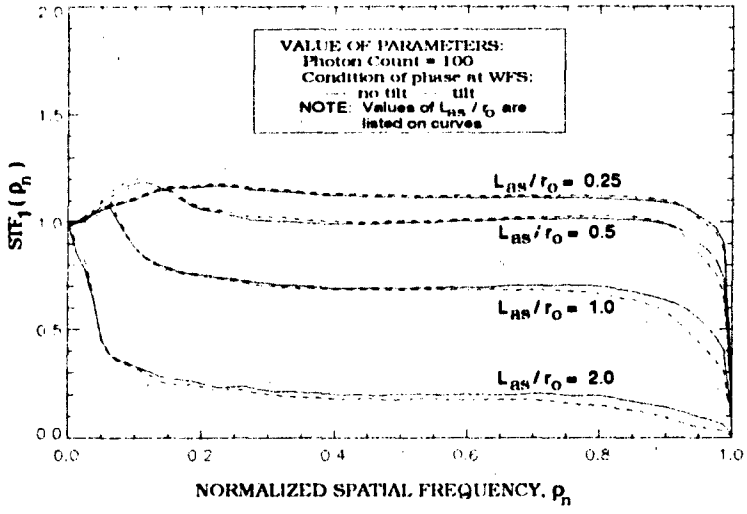

Figure 4.6. STF_1 curves for different wave front sampling conditions as specified by $\frac{L_{as}}{r_o}$, and for tilt and no tilt removed.

$$+j\left\{S_{\mathcal{I}m}(\vec{\rho})\mathcal{N}_{\mathcal{R}e}(\vec{\rho}) - S_{\mathcal{R}e}\mathcal{N}_{\mathcal{I}m}(\vec{\rho})\right\}. \tag{4.5}$$

As will be shown later, the only significant noise term contributing to an STF numerator bias is $S_{\mathcal{R}e}(\vec{\rho})\mathcal{N}_{\mathcal{R}e}$. So, $\langle S(\vec{\rho})S^*\rangle$ can be written as:

$$\langle S(\vec{\rho})S^*(\vec{\rho})\rangle = \langle S^2_{\mathcal{R}e}\rangle + \langle S_{\mathcal{R}e}(\vec{\rho})\mathcal{N}_{\mathcal{R}e}(\vec{\rho})\rangle + \langle S^2_{\mathcal{I}m}\rangle. \tag{4.6}$$

The complex STF denominator term ($|S|^2$) is derived by taking the squared magnitude of equation (4.2) to give:

$$|S(\vec{\rho})|^2 = S^2_{\mathcal{R}e}(\vec{\rho}) + 2S_{\mathcal{R}e}(\vec{\rho})\mathcal{N}_{\mathcal{R}e}(\vec{\rho}) + \mathcal{N}^2_{\mathcal{R}e}(\vec{\rho}) + S^2_{\mathcal{I}m}(\vec{\rho}) + 2S_{\mathcal{I}m}(\vec{\rho})\mathcal{N}_{\mathcal{I}m}(\vec{\rho}) + \mathcal{N}^2_{\mathcal{I}m}(\vec{\rho}). \tag{4.7}$$

The significant bias terms in the denominator are $2S_{\mathcal{R}e}\mathcal{N}_{\mathcal{R}e}$ and $\mathcal{N}^2_{\mathcal{R}e}$ so that $\langle|S(\vec{\rho})|^2\rangle$ can be written as:

$$\langle|S(\vec{\rho})|^2\rangle = \langle S^2_{\mathcal{R}e}(\vec{\rho})\rangle + 2\langle S_{\mathcal{R}e}(\vec{\rho})\mathcal{N}_{\mathcal{R}e}(\vec{\rho})\rangle + \langle\mathcal{N}^2_{\mathcal{R}e}(\vec{\rho})\rangle + \langle S^2_{\mathcal{I}m}(\vec{\rho})\rangle. \tag{4.8}$$

A comparison of equations (4.6) and (4.8) leads to a convenient figure of merit fc ɔn-biased STF performance as those spatial frequencies over which the numerator bias term is eq or less than the denominator bias terms. This approach yields the following inequality:

$$\underbrace{\langle S_{\mathcal{R}e}(\vec{\rho})\mathcal{N}_{\mathcal{R}e}(\vec{\rho})\rangle}_{\text{numerator bias term}} \leq 2\underbrace{\langle S_{\mathcal{R}e}(\vec{\rho})\mathcal{N}_{\mathcal{R}e}(\vec{\rho})\rangle + \langle \mathcal{N}^2_{\mathcal{R}e}(\vec{\rho})\rangle}_{\text{denominator bias term}} \tag{4.9}$$

The range for a non-biased estimator is easily determined by plotting $\langle \mathcal{N}^2_{\mathcal{R}e}(\vec{\rho})\rangle / |2\langle S_{\mathcal{R}e}(\vec{\rho})\mathcal{N}_{\mathcal{R}e}(\vec{\rho})\rangle|$ and noting where the ratio goes above 0.5.

The mean valued results $\langle \mathcal{N}_{\mathcal{R}e}\rangle$ and $\langle \mathcal{N}_{\mathcal{I}m}\rangle$ are plotted in Figure 4.7 for a photon count of 10, and a sampling ratio of 0.25. Notice that only the real part ($\mathcal{N}_{\mathcal{R}e}$) is significant. The results show the real noise term is negatively biased. The imaginary part is many orders of magnitude less, appearing as a straight line in Figure 4.7.

The noise bias problem in the denominator is shown in Figure 4.8. Since the real part of the complex noise is negatively biased, the $2\langle S_{\mathcal{R}e}\mathcal{N}_{\mathcal{R}e}\rangle$ noise term in equation (4.7) is the most significant since it involves the cross product between the negatively biased noise term and the larger and positive real part of S ($S_{\mathcal{R}e}$). $2\langle S_{\mathcal{R}e}\mathcal{N}_{\mathcal{R}e}\rangle$ is easily identified as the noise term most responsible for decreasing the magnitude of the STF denominator. This is easily seen in Figure 4.8, where $2\langle S_{\mathcal{R}e}\mathcal{N}_{\mathcal{R}e}\rangle$ is plotted versus all denomoinator noise terms (terms with $\mathcal{N}_{\mathcal{R}e}$ or $\mathcal{N}_{\mathcal{I}m}$ in them) in equation (4.7). The $\langle \mathcal{N}^2_{\mathcal{R}e}\rangle$ term is the dominant term that causes the denominator bias to decrease slightly.

For the numerator, the complex portion of equation (4.5) essentially averages to zero. Of the real numerator noise terms, only the $\langle S_{\mathcal{R}e}\mathcal{N}_{\mathcal{R}e}\rangle$ term is significant as shown in Figure 4.9. The curve for all real numerator noise terms and just $\langle S_{\mathcal{R}e}\mathcal{N}_{\mathcal{R}e}\rangle$ are almost overlapping. A comparison of Figures 4.9 and 4.8 shows the numerator noise terms contribute slightly over half the negative bias as the denominator noise terms for these photon and sampling conditions. Since both noise

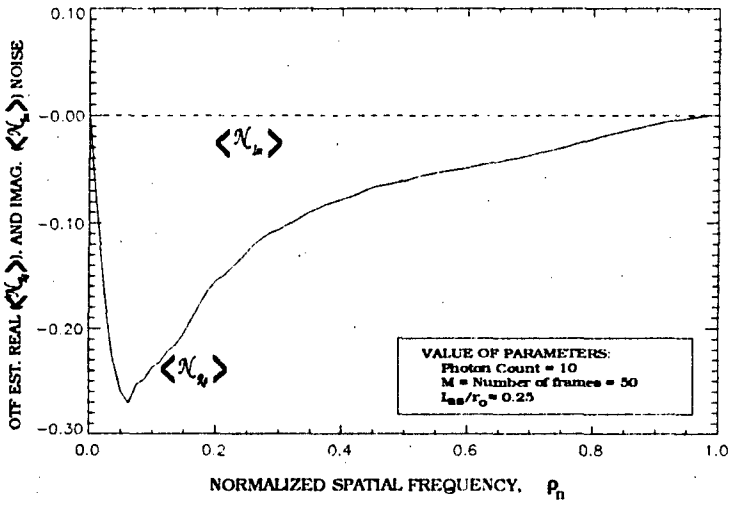

Figure 4.7. OTF estimate ($\hat{S}$) real and imaginary noise content, at a samping ratio of $\frac{L_{ss}}{r_o} = 0.25$ and a photon count of 10.

term contributions are negative, this difference between the numerator and denominator is what makes the STF estimate go above one.

The last part of the noise analysis is to define valid unbiased regions for simulation STF results. The ratio $\frac{\langle \mathcal{N}^2_{Re}(\vec{\rho}) \rangle}{|2\langle S_{Re}(\vec{\rho}) \mathcal{N}_{Re}(\vec{\rho}) \rangle|}$ is plotted in Figure 4.10. Where this ratio goes above 0.5 is where the denominator bias is less than the numerator bias. This will define the non-biased estimator for this thesis. For a sampling ratio of $\frac{L_{ss}}{r_o} = 2$, the criterion used indicates the STF will be unbiased from a normalized spatial frequencey of 0.05 out to the diffraction limit. At a unity sampling ratio ($\frac{L_{ss}}{r_o} = 1$), the unbiased STF is defined from approximately a normalized spatial frequency of 0.09 out to the diffraction limit. At a sampling ratio of $\frac{L_{ss}}{r_o} = 0.5$, the estimator is unbiased from about 0.3 on out to the diffraction limit. This sampling ratio is right on the edge of being biased out to the diffraction limit as seen by how close the ratio $\frac{\langle \mathcal{N}^2_{Re}(\vec{\rho}) \rangle}{|2\langle S_{Re}(\vec{\rho}) \mathcal{N}_{Re}(\vec{\rho}) \rangle|}$ stays to the value of 0.5. For the sampling ratio of 0.25, the STF essentially remains biased out to near the diffraction limit.

Thesis conclusions and recommendations are discussed in the next chapter.

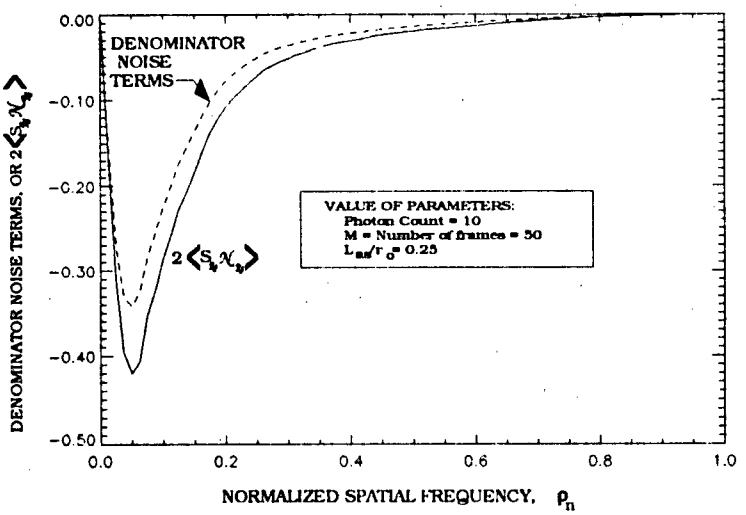

Figure 4.8. STF denominator noise terms versus just $2S_{\mathcal{R}e}\mathcal{N}_{\mathcal{R}e}$, at a samping ratio of $\frac{L_{ss}}{r_o} = 0.25$ and a photon count of 10.

4.5 SNR Results.

The second goal of this thesis is to present single frame SNR results for the two STF's under varying seeing conditions. These single frame SNR estimates characterize, as a function of spatial frequency, the required number of frames of short exposure images and WFS measurements to overcome image reconstruction noise. Only the results for SNR_1 for the case of tilt removed prior to WFS measurements are presented since the same trends were noted whether tilt was or was not removed. SNR_2 behavior is represented by curves for the ratio $\frac{SNR_1}{SNR_2}$. No SNR results are presented for the sampling ratio of 0.25 due to the previously discussed noise bias problem for the STF estimator at that sample ratio. The results are presented in subsections for the sampling ratio conditions of unity sampling ($\frac{L_{ss}}{r_o} = 1.0$), undersampling ($\frac{L_{ss}}{r_o} = 2.0$), and oversampling ($\frac{L_{ss}}{r_o} = 0.5$).

4.5.1 Unity sampling, $\frac{L_{ss}}{r_o} = 1.0$. Estimated single frame SNR_1 results for unity sampling are shown in Figure 4.11. The SNR approaches asymptotic behavior above photon counts of 50, indicating STF_1 is increasingly susceptible to noise at or below this photon count. From the ratio

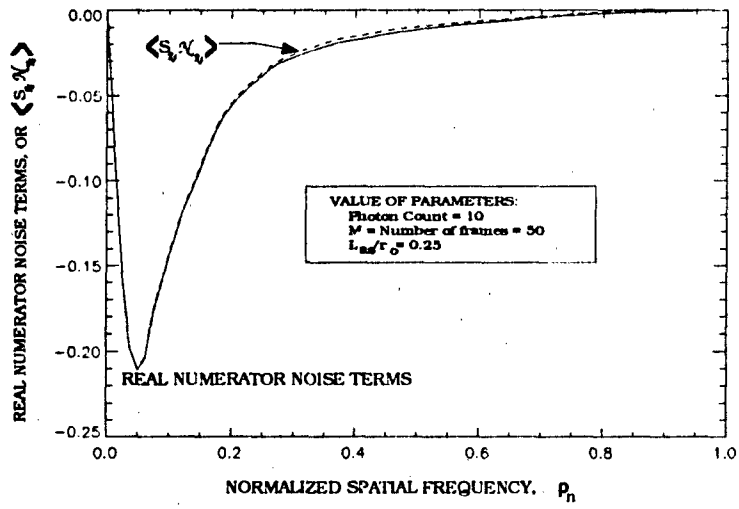

Figure 4.9. STF numerator real noise terms versus just $S_{\mathcal{R}e}\mathcal{N}_{\mathcal{R}e}$, at a sampling ratio of $\frac{L_{as}}{r_o} = 0.25$ and a photon count of 10.

$\frac{SNR_1}{SNR_2}$ curves shown in Figure 4.12, it is evident STF_1 has better SNR characteristics than STF_2 as indicated by the ratio value exceeding one for normalized spatial frequencies above roughly 0.1. There is roughly a factor of 2 difference between SNR_1 and SNR_2 almost out to the diffraction limit of the telescope (normalized spatial frequency of 1.0). One interesting point to note is that the advantage of STF_1 over STF_2, as indicated by the SNR ratio, decreases with increasing photon count. This result indicates that STF_2 is more susceptible to the the higher WFS noise encountered for lower photon counts.

4.5.2 Under sampling, $\frac{L_{as}}{r_o} = 2.0$. Figure 4.13 shows results for SNR_1 for the case of under sampling. The undersampled SNR approaches asymptotic behavior at a photon count exceeding appoximately 100. The asymptotic behavior for the undersampled SNR_1 occurs at higher photon counts than the previously discussed unity sampling case. The undersampled WFS requires higher signal levels to overcome the noise inherent in poorer sampling. The ratio $\frac{SNR_1}{SNR_2}$ curves in Figure 4.14 show that, except for low photon counts and high spatial frequencies, STF_1 is the better method for image reconstruction than STF_2. The advantage of SNR_1 over SNR_2

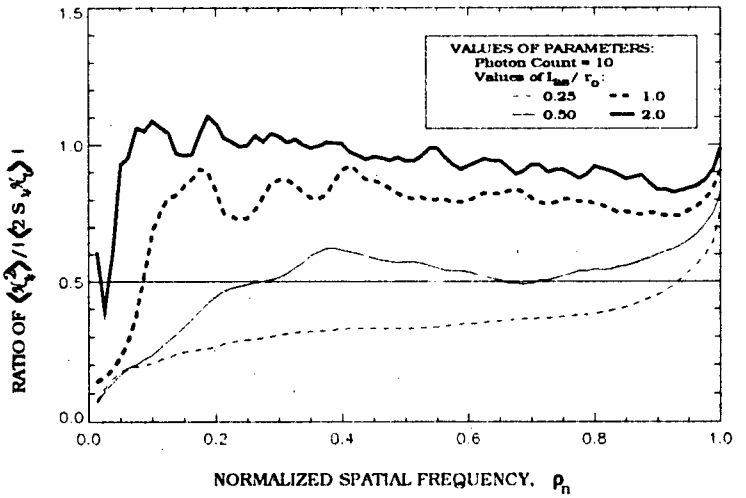

Figure 4.10. Ratio curves for $\frac{\langle \mathcal{N}_{Re}^2(\vec{\rho}) \rangle}{|2\langle S_{Re}(\vec{\rho}) \mathcal{N}_{Re}(\vec{\rho}) \rangle|}$ for a photon count of 10, and varying sampling.

begins at around a normalized spatial frequency of 0.05, with $\frac{SNR_1}{SNR_2}$ approaching 3 for photon counts above 10. For the low photon count of 10 and normalized spatial frequencies approaching unity, the two STF SNRs are roughly equal. The STF_1 image estimator approach is increasingly preferred over STF_2 as the photon counts increases.

4.5.3 Over sampling, $\frac{L_{as}}{r_o} = 0.5$. Only SNR results for a sampling ratio of 0.5 are presented due to the significant STF noise bias STF at a sampling ratio of 0.25. The SNR results for a sampling ratio of 0.5 are shown in Figure 4.15 for SNR_1. As expected, the SNR_1 curves are higher than the previously considered under ($\frac{L_{as}}{r_o} = 2$) and unity ($\frac{L_{as}}{r_o} = 1$) sampling cases. The better results are due to a more accurate phase estimate, leading to better STF estimator performance, particularly at higher spatial frequencies. Additionally, the advantage of the STF_1 over the STF_2 estimator decreases with increasing photon count, as evidenced by $\frac{SNR_1}{SNR_2}$ curves approaching unity for higher photon counts in Figure 4.16. What this essentially means is that the STF_1 and STF_2 estimators are equally good for image reconstruction for an adequate signal, and a good sampling ratio.

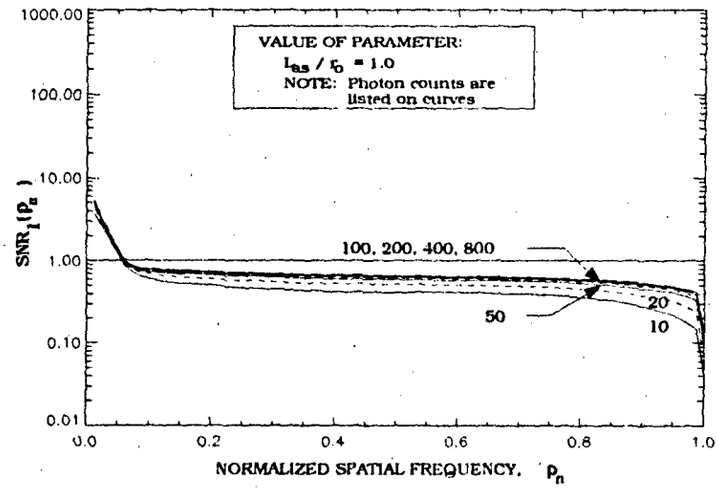

Figure 4.11. Tilt removed SNR_1 curves for wave front sampling conditions at $\frac{l_{as}}{r_o} = 1.0$.

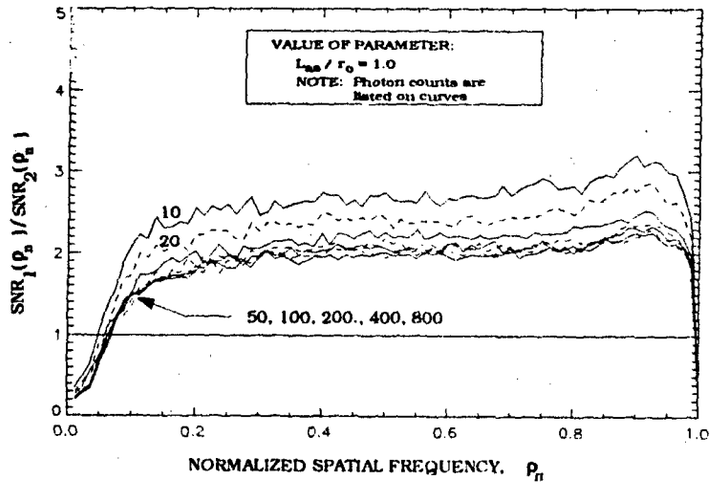

Figure 4.12. Tilt removed $\frac{SNR_1}{SNR_2}$ curves for wave front sampling conditions at $\frac{l_{as}}{r_o} = 1.0$.

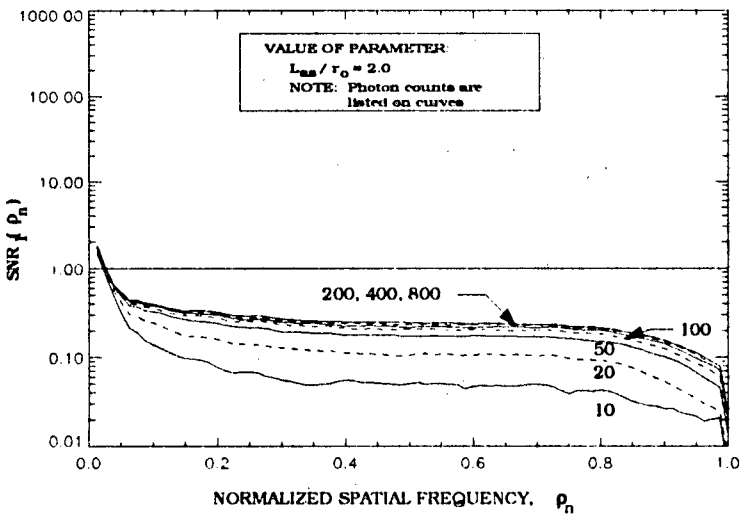

Figure 4.13. Tilt removed SNR_1 curves for wave front sampling conditions at $\frac{L_{ea}}{r_o} = 2.0$.

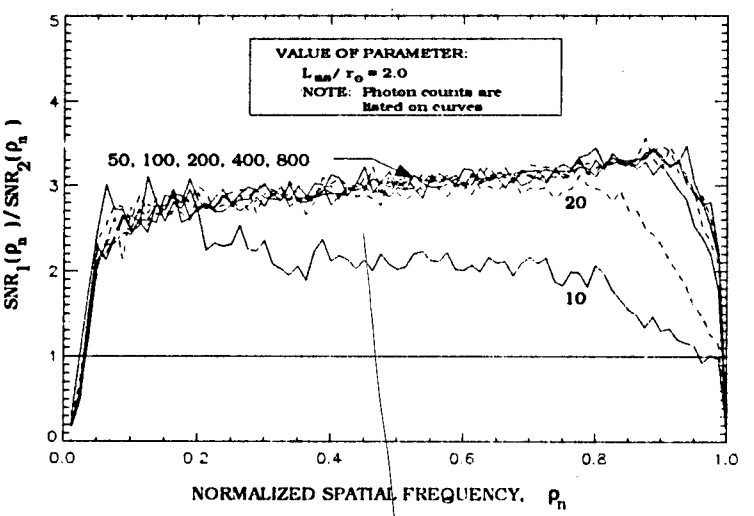

Figure 4.14. Tilt removed $\frac{SNR_1}{SNR_2}$ curves for wave front sampling conditions at $\frac{L_{ea}}{r_o} = 2.0$.

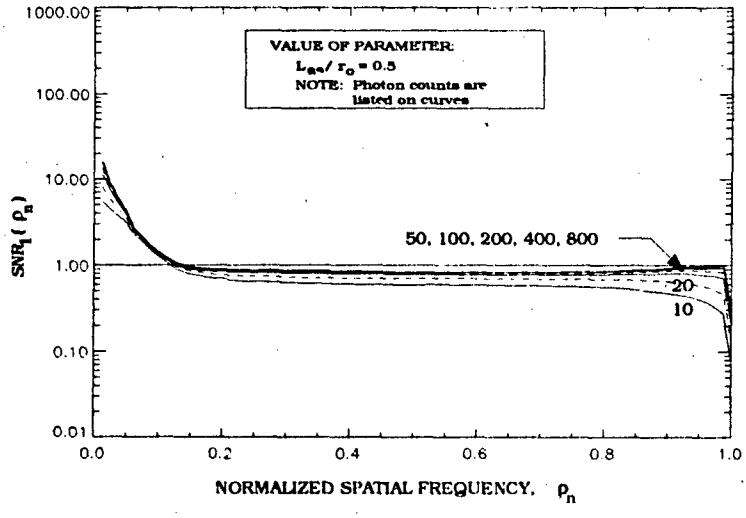

Figure 4.15 Tilt removed SNR_1 curves for wave front sampling conditions at $\frac{L_{aa}}{r_o} = 0.5$.

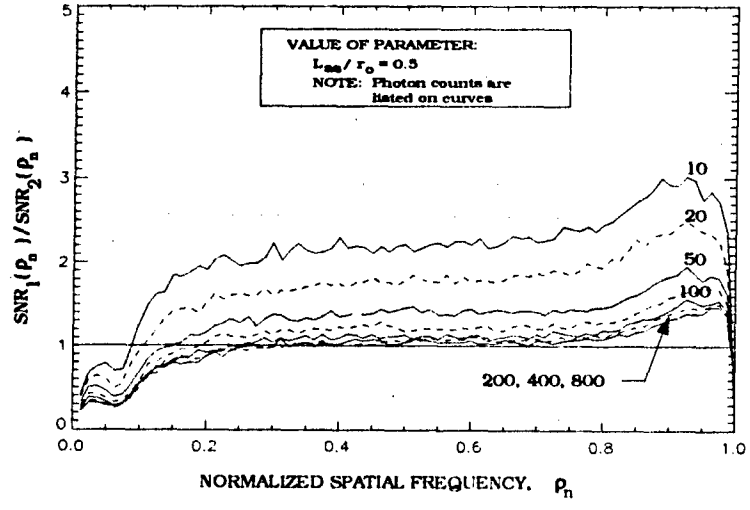

Figure 4.16. Tilt removed $\frac{SNR_1}{SNR_2}$ curves for wave front sampling conditions at $\frac{L_{aa}}{r_o} = 0.5$.

V. Conclusions and Recommendations.

5.1 Conclusions.

This thesis is a follow-on to a previous analytic investigation of the STF for the SRSH image reconstruction technique. The thesis objective was to characterize two different estimator approaches, STF_1 and STF_2, and to compare the signal-to-noise ratios (SNRs) to determine which technique was most advantageous for image reconstruction. The simulation SNRs were also included to provide a means to determine frame requirements to achieve a desired image reconstruction SNR. The most significant result for this thesis, however, was the isolation of a noise bias in the OTF estimate, S.

Ignoring for a moment the bias problem encounted in the simulation, the non-biased results followed trends established by earlier analytic results [24]. In general, the STF can be improved with increased signal strength (characterized by the average photon count per subaperture per short exposure image,N) up to an asymptotic limit determined by the wave front sensor (WFS) sampling ratio ($\frac{L_{as}}{r_o}$). Some additional are the STF is extremely sensitive to variations in the sampling ratio for a fixed signal strength, and can be significantly boosted by improving the sampling ratio. Finally, tilt removal prior to WFS measurements made a slight improvement on image reconstruction, but was not as significant as improving the signal strength or the sampling ratio.

In comparing the two approaches to image reconstruction, STF_1 is easily the better method as shown by the $\frac{SNR_1}{SNR_2}$ curves remaining more or less above unity value for most conditions considered. The advantage of STF_1 is greatest for under ($\frac{L_{as}}{r_o} = 2$) and unity ($\frac{L_{as}}{r_o} = 1$) sampling conditions as seen by $\frac{SNR_1}{SNR_2}$ curves remaining above unity for much of the spatial frequency range out to the diffraction limit. Under good sampling ($\frac{L_{as}}{r_o} = 0.5$), STF_1 approached STF_1 performance, particularly at higher photon counts ($N \geq 200$). Because of the significant bias problem at the sampling ratio of 0.25, it was not determined at which point STF_2 actually outperforms STF_1 under very good sampling conditions.

Perhaps the most important conclusion for this thesis is that the SRSH method is degraded by a bias. In trying to isolate and characterize an apparent bias problem with STF curves, a careful analysis of the OTF estimate ($\hat{S}$) showed the problem of STF curves exceeding the theoretical maximum result of unity, was due to a negative bias ($\langle \mathcal{N}_{\mathcal{R}e} \rangle$) in $\hat{S}$. By carefully examining noise terms in both the STF numerator ($S\hat{S}^*$) and denominator ($|\hat{S}|^2$), a useful noise bias figure of merit was developed for determining non-biased ranges for the STF curves. The figure of merit is the ratio of the positive numerator bias term to the absolute value of the dominant denominator bias term ($\frac{\langle \mathcal{N}^2_{\mathcal{R}e}(\vec{\rho}) \rangle}{|2\langle S_{\mathcal{R}e}(\vec{\rho}) \mathcal{N}_{\mathcal{R}e}(\vec{\rho}) \rangle|}$). This ratio was used to characterize regions of minimal bias. Basically, the threshold value for this figure of merit occurs when the numerator and denominator bias terms are identical (value of 0.5 for $\frac{\langle \mathcal{N}^2_{\mathcal{R}e}(\vec{\rho}) \rangle}{|2\langle S_{\mathcal{R}e}(\vec{\rho}) \mathcal{N}_{\mathcal{R}e}(\vec{\rho}) \rangle|}$).

5.2 Recommendations.

The results from this thesis clearly point toward the need to develop a non-biased estimator. The bias problem can be minimalized by subtracting off appropriately calculated bias terms at the end. However, a better approach would be to develop a non-biased OTF estimate, or modify the filtering (Wiener filter). As a first step, the negatively biased noise in $\hat{S}$ should be studied further to characterize the influence of photon count and sampling ratio values on STF bias levels.

As a final note, some SRSH simulation runs should be done using the minimum variance control law for phase reconstruction, since this was the control law used for the previous analytic approach [24].

Appendix A. Selected Numerical Methods From the Simulation.

A.1 Karhunen-Loève-Fast-Fourier-Transform (KL-FFT) Method of Phase Screen Generation.

This section summarizes pertinent information from an unpublished report by Cochran [17]. The technique used by the simulation to generate random phase screens involves an inverse Fourier transform of filtered complex Gaussian random variables, followed by correction of low order spatial frequenies with a limited number of orthogonal Karhunen-Loève functions. This technique is called the Karhunen-Loève-Fast-Fourier-Transform (KL-FFT) Method of Phase Screen Generation. For the simulation, the FFT portion creates a 128 x 128 pixel array as represented by the solid lined outer box in Figure A.1. The x-y axes are centered at row and column location (65, 65), and is oriented as shown. KL corrections occur over a circular region with a diameter encompassing 129 pixels. A dotted line on the lower and right sides of the outer box of Figure A.1 indicates this circle of correction extends one row or column beyond the defined boundaries of the FFT array. The random phase screens used for individual frames of the simulation originate from the center 81 x 81 pixels as indicated by the inner solid lined box. The KL-FFT method generates a complex screen, of which the real portion is used on odd frames, and the imaginary portion on even frames.

A.1.1 FFT generated phase screen. Complex phase screen generation begins with the 128 x 128 pixel array being loaded with box-muller transform (see Section A.2) generated complex gaussian numbers, $\tilde{z}(\vec{x}) = z_1(\vec{x}) + jz_2(\vec{x})$. The real and imaginary parts of $\tilde{z}$ are zero mean Gaussian random variables with a standard deviation of one. The resulting random array is then filtered by the spatial filter defined by [17:2]:

$$\mathcal{H}(\vec{x}) = \begin{cases} \left[0.1517\left(\sqrt{\vec{x}}\right)^{\frac{-11}{6}}\right] & \text{if } |\vec{x}| > 0, \text{ and} \\ 0 & \text{otherwise,} \end{cases} \tag{A.1}$$

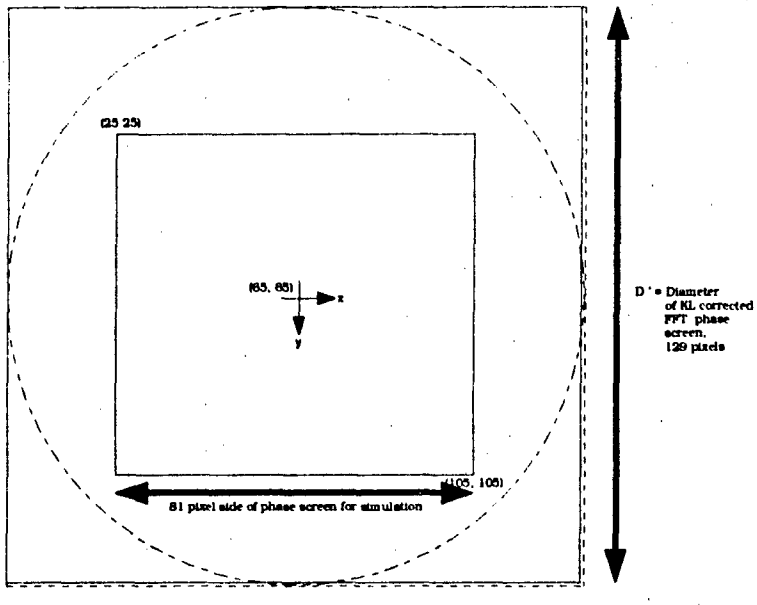

Figure A.1. Location of phase corrections.

where $\mathcal{H}$ is the spatial filter, and $\vec{x}$ is the spatial position. The FFT estimate of a complex phase screen is generated by the inverse Fourier transform of this filtered array:

$$\tilde{\Psi}_{fft}(\vec{x}) = \mathcal{F}^{-1}\left\{\mathcal{H}(\vec{x})[z_1(\vec{x}) + jz_2(\vec{x})]\right\}, \tag{A.2}$$

where $\tilde{\Psi}_{fft}$ represents the complex FFT phase screen. The next step is to boost the low frequency components of this screen through addition of appropriately scaled KL functions.

A.1.2 KL correction to FFT generated phase screen. Two low order KL functions are used to correct tilt in the FFT phase screens. First, a random strength is generated for each KL function to be added to the FFT estimate of the phase screen. The box–muller transform generates a gaussian random number, $\tilde{y}_i = y_1 + jy_2$, with zero mean and variance determined by the Zernike covariance matrix method, for scaling the ith KL function. The amount of correction required for the ith KL function is found by subtracting the normalized inner product of the KL function with

the phase screen from this complex number:

$$\tilde{\gamma}_i = \tilde{y}_i - \left\{ \frac{\sum_{x_i} \sum_{y_i} \tilde{\Psi}_{fft}(\vec{x}) K_i(\vec{x})}{\sum_{x_i} \sum_{y_i} [K_i(\vec{x})]^2} \right\}, \tag{A.3}$$

where $\tilde{\gamma}_i$ is the complex scaler strength of the correction required for the ith KL function. The correction of the wave front, $\tilde{\Psi}_{fft}$, for the KL functions is then given by:

$$\tilde{\Psi}_{kl-fft}(\vec{x}) = \tilde{\Psi}_{fft}(\vec{x}) + \sum_i \tilde{\gamma}_i K_i(\vec{x}), \tag{A.4}$$

where $\tilde{\Psi}_{kl-fft}$ is the KL-FFT complex phase screen.

Next, the real (odd frame numbers) or imaginary (even frame numbers) part of the center 81×81 pixels of $\tilde{\Psi}_{kl-fft}$ is scaled for turbulence strength through use of the Fried parameter, r_o. The resulting real random phase screen is given by:

$$\phi(\vec{x}) = \left[\frac{128.0 \Delta x}{r_o} \right]^{\frac{5}{6}} \underbrace{[\mathcal{R}e \text{ or } \mathcal{I}m\{\tilde{\Psi}_{kl-fft}(\vec{x})\}]}_{\text{center } 81 \times 81 \text{ pixels}}, \tag{A.5}$$

where $\mathcal{R}e$ signifies the real and $\mathcal{I}m$ the imaginary part of $\tilde{\Psi}_{kl-fft}$, Δx is the distance between pixels in the aperture. This phase screen, ϕ, is used in the simulation as the uncorrected phase front.

A.2 Box-Muller transform.

The box-muller transform generates two gaussian random numbers of zero mean and standard deviation σ. The transform is defined as:

$$z_1(\vec{x}) = \sigma \sqrt{-2.0 \ln \zeta_1} \cos(2\pi\zeta_2) \tag{A.6}$$

$$z_2(\vec{x}) = \sigma \sqrt{-2.0 \ln \zeta_1} \sin(2\pi\zeta_2), \tag{A.7}$$

where ζ_1 and ζ_2 are random numbers between zero and one, and z_1 and z_2 are the zero mean gaussian random numbers.

A.3 Karhunen-Loève (KL) Representation of a Random Phase Screen.

The KL correction to the FFT phase screen originates from the technique of using a series representation for a random phase screen. The expression for the random phase front in a circular aperture is given as [17:3]:

$$\Psi_{kl}(\vec{r}) = \sum_i y_i K_i(\vec{r}), \tag{A.8}$$

where Ψ_{kl} is KL generated phase screen, K_i is the ith orthogonal KL function, and y_i is the expansion coefficient that contains the turbulence statistics.

A.3.1 Basis functions for a KL expansion. This section summarizes pertinent information from an unpublished report by Cochran [17]. In order to correctly construct a random phase screen, the basis functions used must be orthogonal. One possible set of basis functions for use in constructing random phase aberrations in a pupil are the so-called zero-mean normalized Zernike polynomials. These functions are defined by:

$$Z_p(\vec{r}) = \begin{cases} \sqrt{2(n+1)}\mathcal{R}_n^m(\vec{r})\cos(m\pi), & p \text{ odd, and } m \neq 0, \\ \sqrt{2(n+1)}\mathcal{R}_n^m(\vec{r})\sin(m\pi), & p \text{ even, and } m \neq 0, \\ \sqrt{n+1}\mathcal{R}_n^0, & m = 0, \end{cases} \tag{A.9}$$

where ! signifies a factorial operation, m and n are indices of the Zernike polynomials, p is the identification number of the polynomial according to Noll's system [25:207–208], and $\mathcal{R}_n^m$ is defined by:

$$\mathcal{R}_n^m(\vec{r}) = \sum_{s=0}^{\frac{(n-m)}{2}} \left\{ \frac{\left[(-1)^s(n-1)!(|\vec{r}|)^{n-2s}\right]}{\left[s!\left(\frac{n+m}{2}-s\right)!\left(\frac{n-m}{2}-s\right)!\right]} \right\}. \tag{A.10}$$

where $m \leq n$, and $n-|m|$ is even. The problem with Zernike polynomials is they are not orthogonal functions, with non-zero correlations existing between various polynomials. So although they are ideal for describing phase aberrations, they cannot be used as basis functions for a random phase screen.

The KL technique uses an expansion of the Zernike polynomials to form orthogonal KL functions. Each KL function contains correlated Zernike polynomials. The technique involves first finding the eigenvectors and eigenvalues of the covariance matrix for a basis set of Zernike polynomials. A KL function is constructed from a single eigenvector, whose elements are used to scale the appropriate Zernike polynomials. The eigenvalue determines the variance of the KL function.

The Zernike expansion for the ith KL function is determined from the normalized covariance matrix as follows:

$$Ce_i = \sigma_i^2 e_i, \tag{A.11}$$

where C is the normalized Zernike covariance matrix for the basis set of zernike polynomials, e_i is the ith eigenvector of C, and σ_i^2 is the ith eigenvalue. The elements of the covariance matrix are calculated as follows [26:1175], [17:12]:

$$C_{pp'} = \left\{ \frac{0.15337(-1)^{(n+n'-2m)}\sqrt{(n+1)(n'+1)}\Gamma(\frac{17}{3})\Gamma(\frac{n+n'-\frac{5}{3}}{2})}{\Gamma(\frac{n'-n+\frac{17}{3}}{2})\Gamma(\frac{n+n'+\frac{23}{3}}{2})\Gamma(\frac{n-n'+\frac{17}{3}}{2})} \right\} \delta_{\alpha\alpha'}\delta_{aa'}, \tag{A.12}$$

where $C_{pp'}$ is the covariance between numbered Zernike polynomials p and p' [25:207-208], n and m are indices used for calculating the Zernike polynomials, $\Gamma(\cdot)$ is the gamma function defined by [27:386]:

$$\Gamma(n) = \int_0^\infty \exp(-x)x^{n-1}dx, \tag{A.13}$$

and $\delta_{\alpha\alpha'}$ and $\delta_{aa'}$ are Kronecker delta functions defined as [28:153]:

$$\delta_{aa'} = \begin{cases} 1 & \text{if } a = a' \\ 0 & \text{otherwise.} \end{cases} \tag{A.14}$$

The ith KL function is constructed from the ith eigenvector e_i by the following expansion:

$$K_i(\vec{x}) = \sum_p e_{ip} Z_p(\vec{x}), \tag{A.15}$$

where p is the designator for a particular Zernike polynomial Z_p, and e_{ip} is the pth component of the eigenvector e_i. The phase screen is found by summing over all appropriately scaled KL functions considered:

$$\Psi_{kl}(\vec{x}) = \sum_i \sum_p y_i e_{ip} Z_p \left(\frac{\vec{x}}{\frac{D}{2}} \right), \tag{A.16}$$

where D is the diameter of the pupil, and y_i is a zero mean Gaussian random variable with variance σ_i^2 (eigenvalue for ith KL function). For the simulation, the two lowest order KL functions and their associated variances (eigenvalues) are calculated as part of the setup portion of the simulation. The correction is applied on odd iterations since screens are created two at a time.

Vita

John Devey received a Bachelor of Science degree in Pulp and Paper Technology from the University of Washington, June 1983. He was commissioned as a lieutenant in the United States Air Force Reserve in December 1984 after attending Officer's Training School. He attended the University of New Mexico from January 1985 to December of 1986 and received a Bachelor of Science degree in Electrical Engineering. He was initiated into Eta Kappa Nu and Tau Beta Pi while at the University of New Mexico. He was next assigned to the 4484th Test Squadron at Tyndall AFB, Florida, in January of 1987 where he was a project manager of F-15 operational testing and was a project engineer for tactical telemetry and drone modification efforts in support of Tactical Air Command requirements. In June 1991 he began a Master of Science degree in Electrical Engineering at the Air Force Institute of Technology, Wright-Patterson Air Force Base, Ohio. He completed his degree requirements in March of 1993.

Permanent address: 18614 89th Avenue N.E.
Bothell, Washington 98011

Bibliography

1. J. D. Gonglewski, "Self-referenced speckle holography," *Optical Engineering Reports*, pp. 1,11, December 1990.
2. E. Hecht, *Optics, 2nd Ed.* Reading, Massachusetts: Addison Wesley, 1987.
3. J. Primot, G. Rousset, T. Marais, and J. C. Fontanella, "Deconvolution of turbulence-degraded images from wavefront sensing," *SPIE Proc.*, vol. 1130, 1989.
4. R. K. Tyson, *Principles of Adaptive Optics.* San Diego, California: Academic Press, Inc., 1991.
5. H. T. Yura, "An elementary derivation of phase fluctuations of an optical wave in the atmosphere," *SPIE Proc.*, vol. 75, pp. 9-15, 1976.
6. A. Tebo, "Adaptive optics: The promise for high resolution," *Optical Engineering Reports*, pp. 1,14, December 1991.
7. J. C. Fontanella, "Wavefront sensing, adaptive optics and deconvolution," in *CFHT Workshop on High Resolution Imaging in Astronomy*, 1984.
8. J. W. Goodman, *Statistical Optics.* New York: John Wiley & Sons, 1985.
9. V. Michau, T. Marais, J. Laurent, J. Primot, J. C. Fontanella, M. Tallon, and J. Fuensalida, "High-resolution astronomical observations using deconvolution form wavefront sensing," in *SPIE proceedings on Propagation Engineering: Fourth in a Series*, vol. 1487, 1991.
10. J. H. Hardy, "Active optics: A new technology for the control of light," *Proc. IEEE*, vol. 66, pp. 651-697, 1978.
11. J. D. Gonglewski, D. G. Voelz, J. S. Fender, D. C. Dayton, B. K. Spielbusch, and R. E. Pierson, "First astronomical application of postdetection turbulence compensation: images of α aurigae, ν ursae majoris, and α geminorum using self-referenced speckle holography," *Appl. Opt.*, vol. 29, pp. 4527-4529, 1990.
12. A. T. Young, "Seeing: Its cause and cure," *Astrophys. J.*, vol. 189, pp. 587-604, 1974.
13. J. W. Goodman, *Introduction to Fourier Optics.* New York: McGraw-Hill Book Co., 1968.
14. J. Primot, G. Rousset, and J. C. Fontanella, "Deconvolution from wave-front sensing: a new technique for compensating turbulence-degraded images," *J. Opt. Soc. Am. A*, vol. 7, pp. 1589-1608, 1990.
15. R. N. VonNiederhausern and B. M. Welsh, "Performance analysis of self-referenced speckle holography," *SPIE Proc.*, vol. 1688, April 1992.
16. R. N. VonNiederhausern, "Performance analysis of the speckle holography image reconstruction technique," Master's thesis, School of Engineering, Air Force Institute of Technology, Wright-Patterson AFB, Oh 45433, December 1991.
17. G. Cochran, "Phase screen generation." Submitted to the Phillips Lab, Kirtland AFB, 1985.
18. B. M. Welsh and C. S. Gardner, "Performance analysis of adaptive optics systems using slope sensors," *J. Opt. Soc. Am. A*, vol. 6, pp. 1913-1923, 1989.
19. M. C. Roggemann, "Optical performance of fully and partially compensated adaptive optics systems using least-squares and minimum variance phase reconstructors," *Computers Elect. Engng*, vol. 18, No. 6, pp. 451-465, 1992.
20. B. L. Ellerbroek, "Comparison of least squares and minimal variance wavefront reconstruction for turbulence compensation in the presence of noise, volume 1: Analysis and results." Submitted to the Phillips Lab, Kirtland AFB, July 1986.

21. P. C. Shields, *Elementary Linear Algebra.* New York: Worth Publishers, Inc., third ed., 1980.

22. J. D. Gaskill, *Linear Systems, Fourier Transforms, and Optics.* New York: John Wiley & Sons, 1978.

23. W. B. Davenport, *Probability and Random Processes.* New York: McGraw-Hill Book Co., Inc., 1970.

24. R. N. VonNiederhausern and B. M. Welsh, "Performance analysis of the self-referenced speckle holography image reconstruction technique." Submitted and accepted for publication in *Applied Optics, March 1993.*

25. *R. J. Noll, "Zernike polynomials and atmospheric turbulence,"* J. Opt. Soc. Am., *vol. 66, pp. 207-211, 1976.*

26. *N. Roddier, "Atmospheric wavefront simulation using zernike polynomials,"* Optical Engineering, *vol. 29, No. 10, pp. 1174-1180, October 1990.*

27. *G. B. Thomas and R. L. Finney,* Calculas and Analytic Geometry. *Reading, MA: Addison-Wesley Publishing Co., fifth ed., 1979.*

28. *S. Karni and W. J. Byatt,* Mathematical Methods in Continuous and Discrete Systems. *New York: Holt, Rinehart and Winston, 1982.*